Journal of Foraminiferal Research, v. 54, no. 1, p. 1–19, January 2024

MORPHOTYPICAL AND GEOCHEMICAL VARIATIONS OF PLANKTIC FORAMINIFERAL SPECIES IN SIBERIAN AND CENTRAL ARCTIC OCEAN CORE TOPS

Maya Prabhakar[1,*], Kaustubh Thirumalai[1,**], Thomas M. Cronin[2], Laura Gemery[2], Elizabeth K. Thomas[3] and Patrick A. Rafter[4]

ABSTRACT

In this work, we utilize a transect of core top, mid- to late Holocene, sediments from the Eastern Siberian Sea to the central Arctic Ocean, spanning gradients in upper-ocean water column properties, to examine regional planktic foraminiferal species abundances and geochemistry. We present species- and morphotype-specific foraminiferal assemblages at these sites and stable isotope analyses of neogloboquadrinids. We find little variation in planktic species populations, and only small variations in *N. pachyderma* morphotype distributions, between sites. Spatial averages of *N. pachyderma* morphotype and *N. incompta* $\delta^{18}O$ values show no significant differences, suggesting a similar calcification depth for all morphotypes of *N. pachyderma* and *N. incompta* across our sites, which we estimate to be between ~ 50–150 m. Values of $\delta^{18}O$ of a group of unencrusted specimens delineate a shallower calcification habitat. *Neogloboquadrina pachyderma-2* Mg/Ca values yield temperatures outside the range of observations using available calibration equations, pointing toward the need for more Arctic-specific Mg/Ca-temperature calibrations.

INTRODUCTION

Polar amplification dictates that Arctic air temperatures will warm faster relative to lower latitudes in response to anthropogenic greenhouse warming. Coupled ocean-atmospheric general circulation models typically show a 2–3x increase (Holland & Bitz, 2003), with new studies showing a 4x average increase (Rantanen et al., 2022), in polar warming relative to the global average at twice the preindustrial atmospheric CO_2 level, which jeopardizes Arctic sea and land ice. Sea ice loss is predicted to be spatially variable and affect atmospheric climate modes such as the North Atlantic Oscillation (Holland & Bitz, 2003; Vihma, 2014).

In addition, near-future Greenland Ice Sheet (GrIS) stability is debated, with concerns that the GrIS may lose mass more quickly than predicted in response to global warming (Schaefer et al., 2016; Rantanen et al., 2022). The impacts of freshwater forcing, from melting Arctic land ice on the Atlantic Meridional Overturning Circulation (AMOC) is actively investigated, but short-term changes in Arctic oceanography could impact ocean circulation across longer timescales; increased freshwater from land ice melt in the Arctic is projected to slow mixing in the North Atlantic (Briner et al., 2020; He & Clark, 2022; Lofverstrom et al., 2022). Studies have also predicted a loss of Arctic ice analogous to early Holocene glacial melt and across other periods of ice sheet instability and suggest that AMOC could be significantly reduced (He & Clark, 2022; Lofverstrom et al., 2022). Therefore, it is imperative we understand how Arctic oceanography, regional land and sea ice distributions, and ocean temperatures have changed in response to past climatic forcing.

Many studies have used planktic foraminifera found in marine sediments as indicators of past climate change in the Arctic Ocean. Planktic foraminifera are ubiquitous, microscopic, marine protists that inhabit upper oceanic waters and build calcareous tests (shells), whose geochemistry and relative species abundances have been the backbone of paleoceanographic reconstructions over the past seventy years. Planktic foraminifera show a large latitudinal diversity gradient (Ruddiman, 1969; Schiebel & Hemleben, 2005), and species diversity decreases at the poles. *Neogloboquadrina pachyderma* (Ehrenberg, 1862) is the dominant planktic species found in polar latitudes, and as such, most high-latitude records of foraminiferal geochemistry typically focus on this species. The species is tolerant of cold temperatures (as low as –3°C) and a range of salinities from 30–69 (Hilbrecht, 1996; Bertlich et al., 2021), and has also been found at subtropical latitudes (Kennett & Srinivasan, 1983). These qualities establish *N. pachyderma* as a widely used indicator of Arctic paleoclimatic change (Kohfeld et al., 1996; Hillaire-Marcel et al., 2004; Risebrobakken & Berben, 2018).

The freezing water temperatures in the Arctic, low productivity, and large salinity gradients create a suboptimal environment for the less common Arctic planktic species *Neogloboquadrina incompta* (Parker, 1962), *Turborotalita quinqueloba* (Natland, 1938), and *Turborotalita humilis* (Brady, 1884; Bond et al., 2001; Darling et al., 2006; Cronin et al., 2014). Therefore, the abundance of these taxa, alongside *N. pachyderma*, are used as a proxy for changes in water mass circulation in the high-latitude oceans (Simstich et al., 2003). *Neogloboquadrina incompta* and *N. pachyderma* appear superficially similar in morphology (except for their coiling direction) but are genetically distinct (Darling et al., 2006; Schiebel & Hemleben, 2017). It is important to note that both species can have a minor proportion of individuals within the population that coil in the opposite direction to their standard orientation (Darling et al., 2006). Whereas *N. pachyderma* is typically sinistral (left-coiling), it can have a limited occurrence of ~ 3% dextral (right-coiling) individuals (Darling et al., 2006). Additionally, there is evidence of higher percentages of aberrant coiling direction in laboratory populations, however it is not currently understood what implications this has on paleontological or modern observations (Davis et al., 2020).

Neogloboquadrina pachyderma abundances and isotopic geochemistry have been shown to reflect upper ocean conditions at marginal Arctic Ocean sites. Plankton tows in the Greenland Sea and Nansen Basin indicate that *N. pachyderma*

[1] Department of Geosciences, University of Arizona, 1040 E. 4th Street Tucson, AZ 85721, USA
[2] U.S. Geological Survey, 12201 Sunrise Valley Dr, Reston, VA, 20192, USA
[3] Department of Geology, 126 Cooke Hall, University at Buffalo, Buffalo, NY, 14620, USA
[4] Department of Earth System Science, Croul Hall, University of California, Irvine, CA, 92697, USA
* Correspondence author. E-mail: mayaprabhakar.sci@gmail.com
** Secondary correspondence author. E-mail: kaustubh@arizona.edu

TABLE 1. List of core sites used in this study. Sites are ordered by proximity to the Bering Strait.

Lab ID	Sample name	Latitude	Longitude	Sampling depth (cm)	Depth (m)	Location	Age (kyr)
SWE13	SWERUS L2-13MC4	76.186	–179.278	0–1	1118	East Siberian Shelf	1.474±15
SWE14	SWERUS L2-14MC4	76.353	176.461	0–1	733	East Siberian Shelf	1.073±30
SWE18	SWERUS L2-18-MC4	76.409	173.879	0–1	349	East Siberian Shelf	0.365±25
SWE22	SWERUS L2-22-MC4	78.224	164.427	0–1	367	East Siberian Shelf	0.884±120
B16C	P1-94-AR-B16C	80.34	–178.71	0–1	1568	Mendeleev Ridge	5.835±45
B20A	P1-94-AR-B20A	83.17	174.11	0–1	3120	Mendeleev Ridge	5.788±35
PS2185	2185-4MUC	87.53	–144.48	1–2	1051	Lomonosov Ridge	5.056±15
B31	P1-94-AR-B31	89.98	40.5	0–1	4180	Eurasian Basin	3.360±15
PS2170	2170-4MUC	87.6	60.9	0–1	4083	Amundsen Abyss	1.427±120

size and geochemistry change with depth, and that the stable oxygen isotope composition ($\delta^{18}O$) of *N. pachyderma* shells is controlled by the temperature and the seawater $\delta^{18}O$ (hereafter $\delta^{18}O_{seawater}$) of the water mass in which they calcify (Bauch et al., 1997; Kohfeld et al., 1996). *Neogloboquadrina pachyderma* $\delta^{18}O$ consistently shows an offset of $\sim$ 1‰ from predicted equilibrium calcite $\delta^{18}O$, which is attributed to 'vital effects' (Bauch et al., 1997; Kohfeld et al., 1996). However, a recent study on small groups (four per measurement) of sub-Arctic foraminifera suggests a relatively minor degree of $\delta^{18}O$ variability (0.11‰) unexplained by temperature and $\delta^{18}O_{seawater}$ (Jonkers et al., 2022). In addition to geochemistry, maximum abundances (relative to depth at a local site) of living *N. pachyderma* follow modern chlorophyll maxima in the water column and have been observed with green cytoplasm, which suggests they consume primary producers in the Arctic (Kohfeld et al., 1996; Bauch et al., 1997). Recent work has identified diatoms as their primary food source in the Arctic, with *N. pachyderma* consuming various species based on availability (Greco et al., 2021).

Relative abundances of *N. pachyderma* and *Turborotalita quinqueloba* have also been proposed to track changes in water mass mixing over geologic time (Risebrobakken & Berben, 2018). Furthermore, *N. pachyderma* $\delta^{18}O$ excursions have been used to define large surface freshwater fluxes in the Arctic Ocean in the Holocene (Poore et al., 1999; Bond et al., 2001). Reconstructions using *N. pachyderma* typically assume stationarity in its calcification preferences. However, the geochemical and morphotypical variability occurring among various *N. pachyderma* specimens and their relationship to calcification depths has not yet been fully explored across the Arctic (Altuna et al., 2018).

Altuna et al. (2018) identified five morphotypes within *N. pachyderma* (termed *Nps-1* through *Nps-5*, following their convention). Previous work has also delineated *N. pachyderma* forms solely into "encrusted" and "nonencrusted" categories (Kohfeld et al., 1996) based on the putative presence of a thick calcite crust. "Encrusted" forms have been repeatedly observed deeper in the water column than "nonencrusted" forms, pointing toward vertical migration as an influence on *N. pachyderma* calcification (Kohfeld et al., 1996; Hillaire-Marcel et al., 2004; Altuna et al., 2018; Tell et al., 2022). While the species itself is often attributed to a range of depth habitats from 0 to 200 m, with maximum abundances around 50–100 m, various morphotypes are hypothesized to live at different depths within that range (Bauch et al., 1997; Volkmann, 2000; Bond et al., 2001; Altuna et al., 2018). Furthermore, the question of depth habitat as it relates to morphotype size has two conflicting hypotheses: one suggests larger forms live deeper in the water column, around 100–200 m, (Hillaire-Marcel et al., 2004), and the other suggests the inverse (Xiao et al., 2014). If morphotypes of *N. pachyderma* indeed calcify at different depths of the water column, they would exhibit different $\delta^{18}O$ values relative to changes in temperature and $\delta^{18}O_{seawater}$ within the water column. Vertical changes are steep in the Arctic Ocean but exhibit spatial variability. Generally, there is a strong halocline between a low-salinity mixed layer influenced by sea ice melt and riverine input versus higher-salinity Atlantic waters. The depth of the halocline would influence *N. pachyderma* $\delta^{18}O$. Thus, it is important to resolve the depths at which *N. pachyderma* and its morphotypes live and calcify across the Arctic Ocean to accurately interpret downcore records. While there is evidence for a relationship between *N. pachyderma* morphotypes, size, and stable isotopic composition in the Canadian Archipelago (Altuna et al., 2018), that environment does not reflect the entirety of Arctic oceanography. Here, we investigate multiple planktic species across mid- to late Holocene sediment obtained from core tops from the eastern and central Arctic Ocean and evaluate the implications of their geochemistry for calcification depth habitat.

MATERIALS AND METHODS

For this study, we used nine core top sediments (0–1 cm and 1–2 cm; Table 1) spanning 76–90°N and 144°W–40°E, along an approximate transect from the Bering Strait toward the Fram Strait via the central Arctic Ocean (Fig. 1, Fig. A1). We obtained temperature and salinity data from the World Ocean Atlas (WOA; Locarnini et al., 2019; Zweng et al., 2019) for the upper 200 m of the water column (Fig. 1, Figs. A2–A4). World Ocean Atlas data are sourced from CTD casts and observations are interpolated to 102 standard depths. The dataset spans 1955 to present with a monthly resolution and has a maximum square grid resolution of 0.25°. In addition to WOA data, we collated CTD data from seven sites close to our core sites (Anderson, 2006; Swift, 2006; Rabe & Wisotzki, 2010; Björk, 2017). We then imaged and analyzed individual tests (Fig. 2), prepared assemblages for species and morphotype abundance (Fig. 3), and calculated benthic-to-planktic abundance ratios. Subsequently, we analyzed the stable isotope geochemistry of multiple neogloboquadrinids (Figs. 4–6), and Mg/Ca in *N. pachyderma* as proxies for temperature and $\delta^{18}O_{seawater}$ (Fig. 7). Bulk dry samples were obtained from the United States Geologic Survey, Florence Bascom Geosciences Center (Table 1). Cores were originally collected during the following cruises: Polarstern Ark-VIII/3, the 1994 Arctic

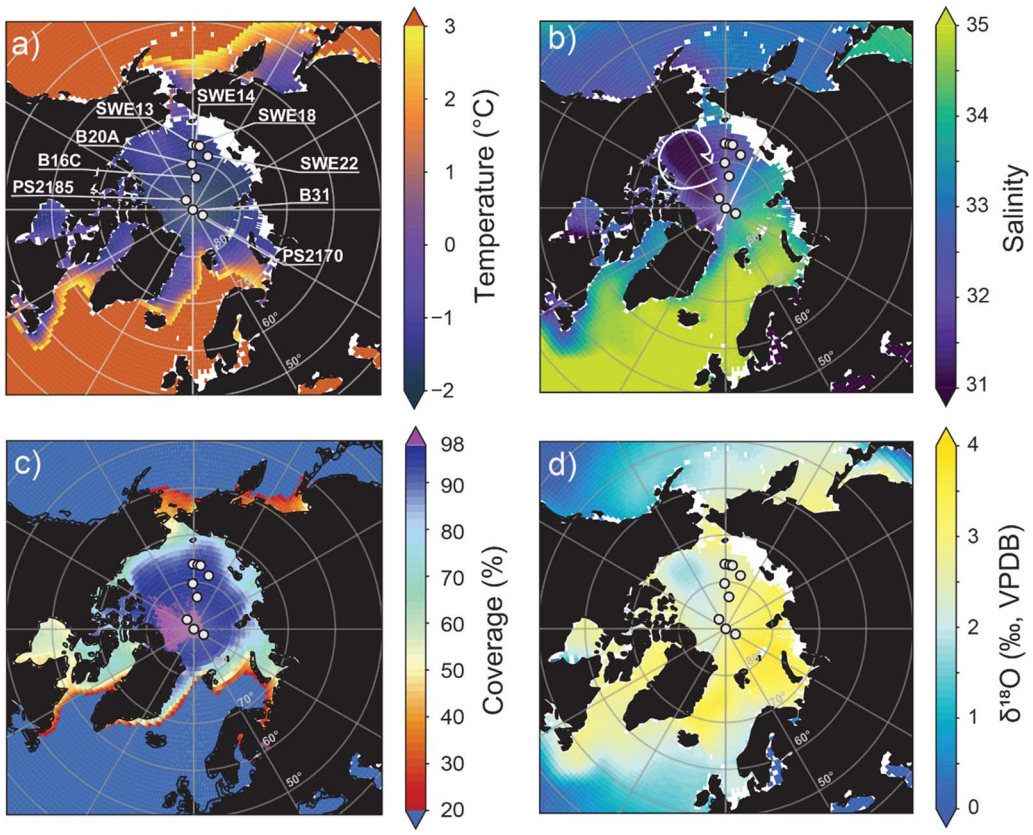

FIGURE 1. Arctic Ocean Climatology including mean annual a) temperature, b) salinity, c) sea ice and d) forward-modeled $\delta^{18}O$ at 50 m. Temperature and salinity were obtained from the World Ocean Atlas (Zweng et al., 2019; Locarnini et al., 2019) and forward-modeled $\delta^{18}O$ was computed using established transfer functions (see Methods for details). Sea ice coverage was taken from the Hadley Center Sea Ice and Sea Surface Temperature (HadISST) dataset (Rayner, 2003), and core-top sites are shown as light green points and labeled according to laboratory identifications (see Table 1). White arrows in (b) indicate major surface currents: the Beaufort Gyre and the Transpolar Drift.

Ocean Section, and the Swedish-Russian-US Arctic Ocean Investigation of Climate-Cryosphere-Carbon Interactions (SWERUS) Leg 2 (The participants of ARK-VIII/3, 1992; Aagaard et al., 1996; SWERUS Scientific Party, 2016). Sediments were dry-sieved using a ≥150-µm sieve and all samples were randomly split into ~1/32 of the original volume using a microsplitter before sorting by size fraction. The samples were then sorted into <150-µm, 150–212-µm, 212–350-µm, and >350-µm size fractions. We obtained radiocarbon dates by picking one milligram of *N. pachyderma* morphotype 2 (*Nps-2*) from the 150–212-µm fraction, which were measured at the Keck Carbon Cycle Laboratory at the University of California, Irvine. We calibrated radiocarbon ages using CALIB REV8.2 with a marine reservoir correction of 238 years (based on Marine20 data) and, using an uncertainty value of 70 years, calculated from the most proximal Arctic Ocean sites in the database (Stuiver & Reimer, 1993; Heaton et al., 2020). All ages in this study are reported in calibrated years before present (1950). The ages of five core-top samples ranged from 0.3–1.5 ka (SWE13, SWE14, SWE18, SWE22, and B31), one sample was dated to 3.4 ka (PS2170), and three others were between 5–5.8 ka (B16C, B20A, and PS2185). We omitted one core top older than 6 ka (not shown in figures) to constrain the temporal range of this study and provide a mid- to late Holocene baseline of foraminiferal assemblages and geochemistry.

Regional Oceanographic Setting & Sampling Domain

Across our sampling domain, the upper 100 m of the Arctic Ocean is relatively cold and exhibits low spatial variability in mean annual temperatures at 50 m (Fig. 1a; see Fig. A1 for contextualized bathymetric features). However, upper Arctic Ocean waters are comprised of a mixture of Pacific and Atlantic waters, as well as continental freshwater input, creating a steep surficial salinity gradient and halocline (Timmermans & Marshall, 2020). Four of our sites are located in the Eastern Siberian Sea where the Kolmya and Indigirka rivers terminate onto the continental slope. Adjacent to the Eastern Siberian Sea, in the Canadian Arctic (Fig. A1), is the much less saline Beaufort Gyre (Fig. 1b), where freshwater influx, circulation conditions, and the formation of sea ice modify sea surface salinity gradients and stratification throughout the year (Timmermans & Marshall, 2020). Although we do not have samples from the Beaufort Gyre, we collate previously published measurements proximal to the Beaufort Sea that allow us to distinguish between the low- and high-salinity regimes (Spielhagen & Erlenkeuser, 1994; Xiao et al., 2014).

Five other samples mark a transect across the central Arctic. Toward the Fram Strait, more saline North Atlantic waters enter the Arctic, influenced by the North Atlantic Current, and flow deeper than North Pacific waters and freshwater influx in the water column (Cronin et al., 2014; Timmermans &

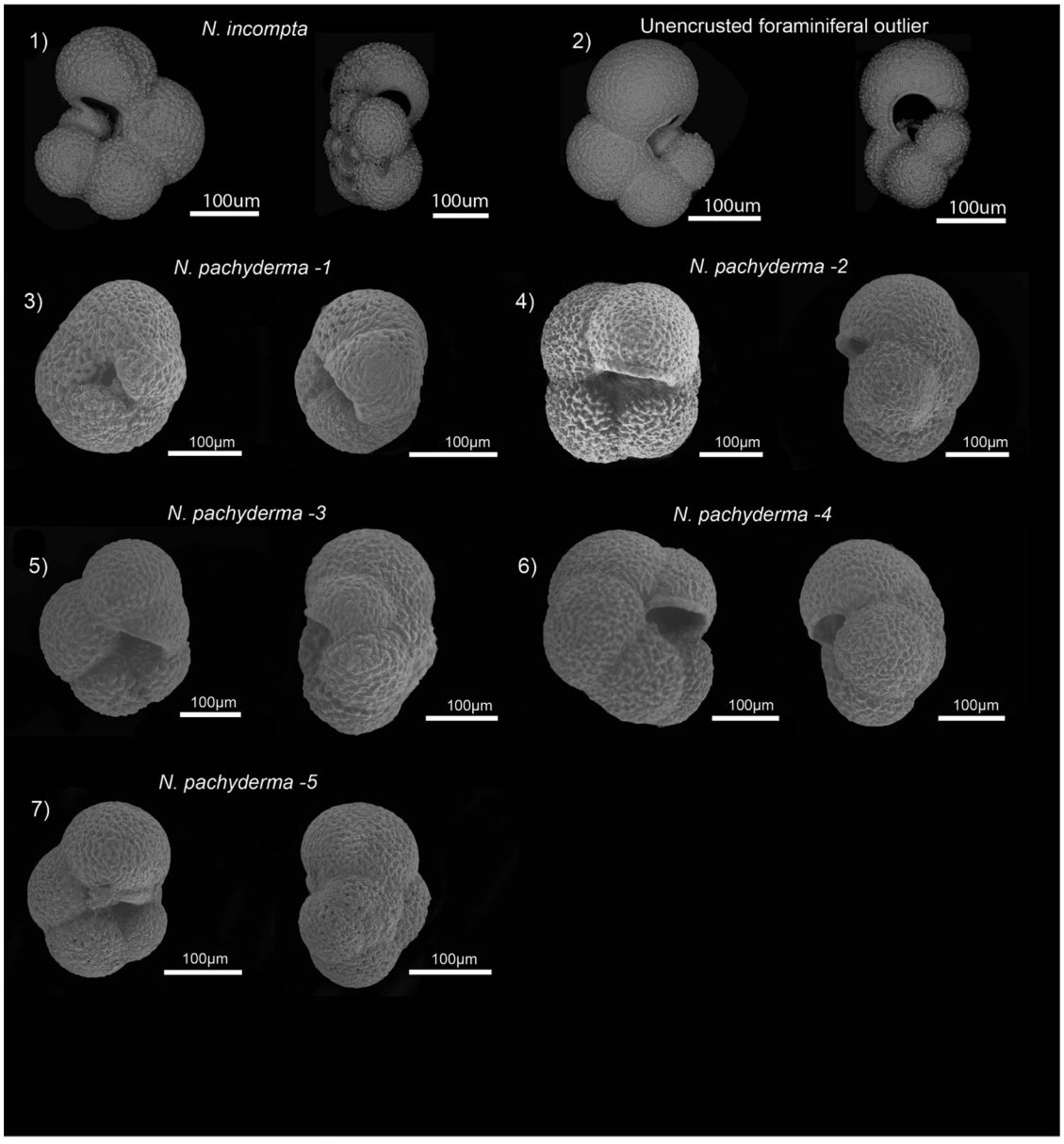

FIGURE 2. Scanning (1, 3–7) and backscatter (2) electron microscopic images showing the umbilical (left) and lateral edge (right) views. **1** *Neogloboquadrina incompta*. **2** an unencrusted foraminiferal outlier. **3** *Neogloboquadrina pachyderma* morphotype 1. **4** *Neogloboquadrina pachyderma* morphotype 2. **5** *Neogloboquadrina pachyderma* morphotype 3. **6** *Neogloboquadrina pachyderma* morphotype 4. **7** *Neogloboquadrina pachyderma* morphotype 5.

Marshall, 2020). The percent contribution of Pacific and Atlantic water to the Arctic water column is correlated with the relative depth of the halocline; as the contribution of Pacific water decreases, the halocline shoals (Timmermans & Marshall, 2020). Central Arctic bathymetry includes the Lomonosov Ridge (Fig. A1), which provides a physical boundary for incoming Atlantic water and roughly marks where Pacific water becomes negligible. In contrast, sea ice meltwater increases its relative contribution to the upper 300 m in the central Arctic Ocean, particularly the Amundsen Basin (Ekwurzel et al., 2001). Riverine influx is consistent in its contribution between the Chukchi Abyssal Plain and the Amundsen Basin, however its relative contribution increases in the central Arctic Ocean (Ekwurzel et al., 2001).

Arctic Ocean temperature in the upper 200 m ranges from approximately –2–0°C and salinity from 30–35 (Fig. 1, Figs. A2–A4). Toward the Bering Sea, where Pacific water is the primary component of the upper 200 m, the Eastern Siberian Sea is comprised of two distinct sections due to the strong lobe of riverine freshwater from Siberia. East of 160°E, the water column is primarily comprised of Pacific water with an average salinity of 29.7–32.2 and temperature of –0.17–0.58°C (Semiletov, 2005). West of 160°E, the water column is dominated by riverine influx with an average salinity of 22.3–24.5 and temperature of 2.23–2.63°C (Semiletov, 2005). The average coverage of sea ice in the Eastern Siberian Sea is approximately 90–100% in March and 0–60% in September (Cavalieri & Parkinson, 2012). Sea ice coverage increases moving toward the northern coast of Greenland

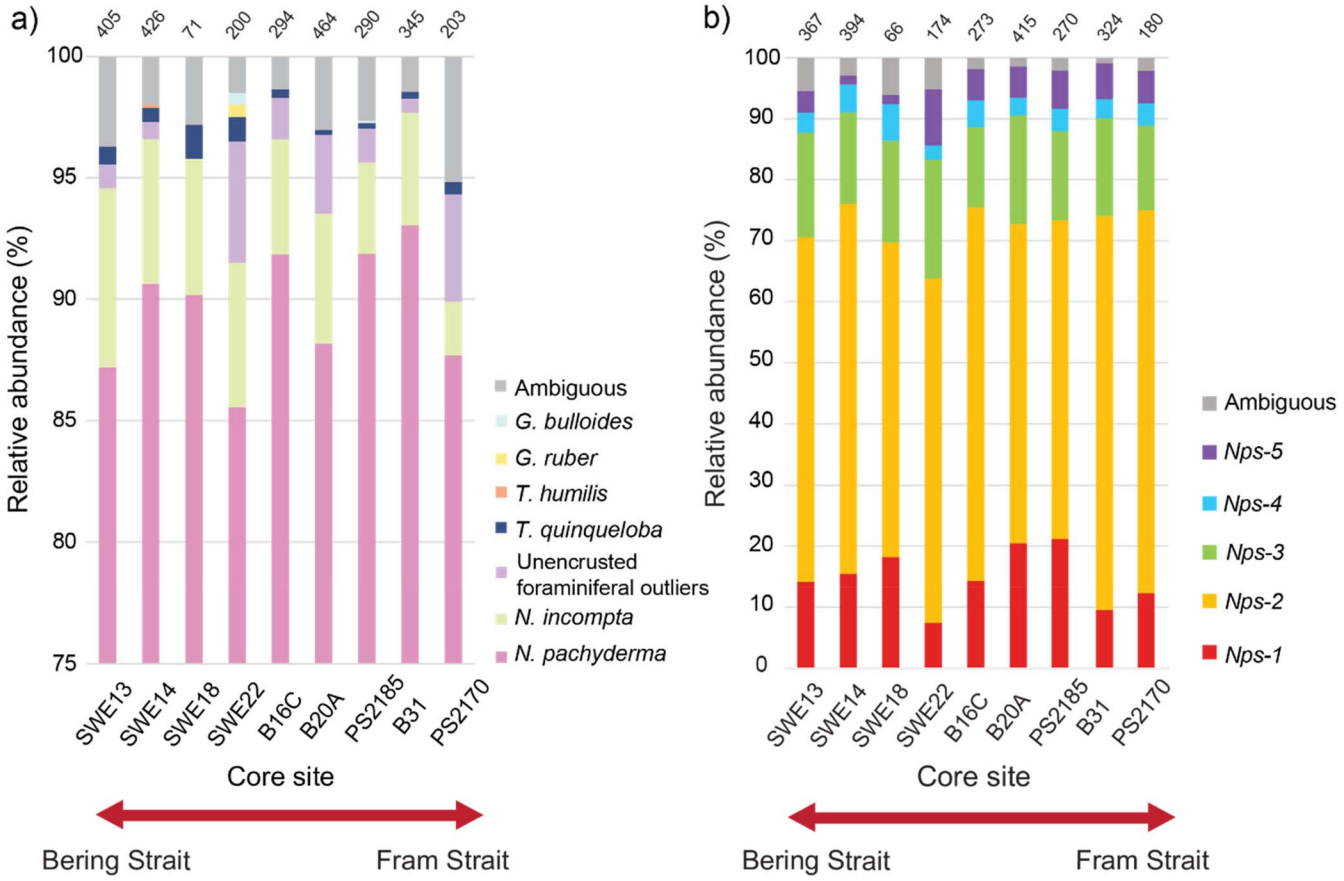

FIGURE 3. a) Relative planktic foraminiferal species abundances across core sites. Total number of planktic specimens is listed at the top of each bar. b) Abundances of *N. pachyderma* morphotypes within populations of *N. pachyderma* (*i.e.,* within the fraction of corresponding values in (a)). The total number of *N. pachyderma* individuals is listed at the top of each bar.

(Fig. 1c) and the central Arctic has an average coverage of 100% in March and 80–95% in September (Cavalieri & Parkinson, 2012). Overall, our sites cover sharp gradients in sea ice coverage and oceanographic properties.

Assessments of Post-Depositional Alteration

Given that not all our core tops preserve modern sediments, we assessed the potential for post-depositional alteration of planktic foraminiferal calcite across the sites. We investigated ultrastructure preservation via micro-imaging techniques wherein we imaged individual tests using a Hitachi 3400N Scanning Electron Microscope at the University of Arizona LaserChron Laboratory. Samples were uncoated and photos were taken at 200–500×, 750×, and 1500× to image the whole test and the underlying ultrastructure. All images are secondary electron images except those of the unencrusted foraminiferal outliers (UFOs; Fig. 2 and Figs. A9–A11), which were backscattered electron (BSE) images. A total of 23 specimens were imaged across the nine core-top samples, where individual tests were randomly selected from assemblages. We evaluated (*N. pachyderma* morphotype) *Nps-2* images across all sites for relative dissolution using preservation descriptions outlined by Romanova et al. (2017) and Consolaro et al. (2015), shown in Figure A5. Specimens were graded on a scale of 1–5, where a grade of 1 consists of total denudation or removal of surface crystals on test crust, large pores, noticeable thinning of ultimate chamber, channeling of aperture lip, and evidence of recrystallization. A grade of 5 consists of sharp pyramidal surficial crystals, an intact aperture lip, thick-walled ultimate chamber, and small pores. Grades between 1 and 5 represent the relative presence of dissolution or recrystallization characteristics (Fig. A5). Additionally, we examined the benthic-planktic ratio as a proxy for preferential dissolution of planktic species between sites (Thunell, 1976; Fig. A5).

Foraminiferal Assemblages and Species' Relative Abundances

We generated foraminiferal assemblages (average n = 317 specimens) at each of our sites and enumerated the relative planktic foraminiferal species abundances and morphotypical abundances of *N. pachyderma* (Figs. 3–4). Abundances were calculated from a randomly split sample fraction prepared prior to size-dependent sorting. We prepared assemblages from randomly sorted fractions of bulk sedimentary core material greater than 150 μm. Planktic species and morphotypes of *N. pachyderma* were identified following Altuna et al. (2018), Schiebel & Hemleben (2017), and Kennett & Srinivasan (1983). *Neogloboquadrina pachyderma* morphotype assemblages were recorded from the same species assemblages. We labelled specimens as "ambiguous" if those individuals contained hybrid characteristics of two distinct

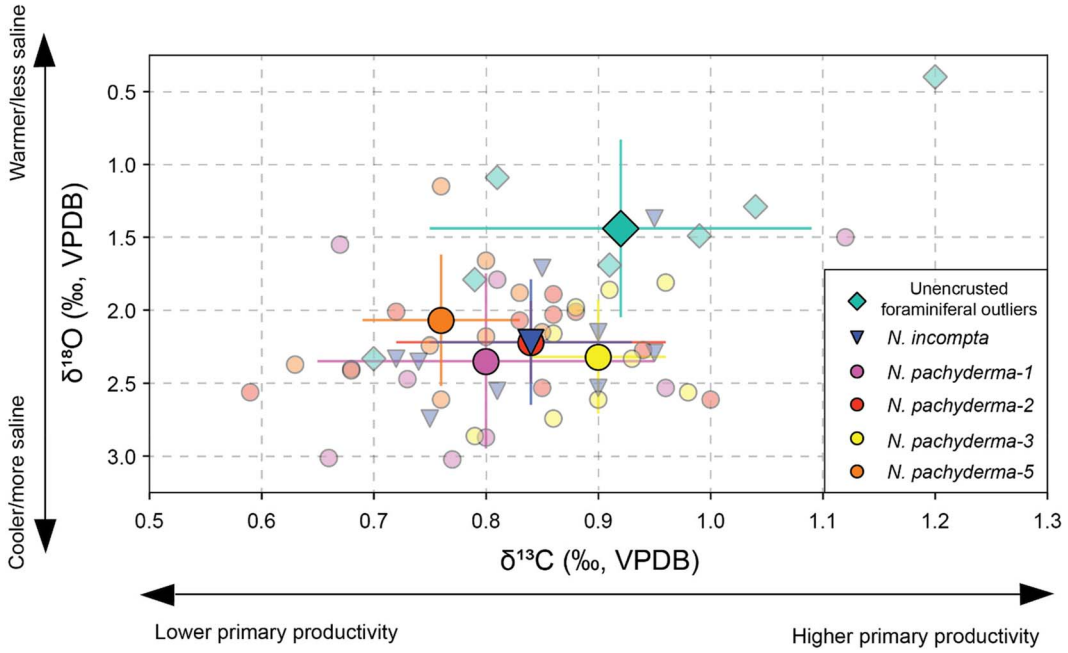

FIGURE 4. Multi-specimen stable carbon and oxygen isotope measurements of *N. pachyderma* morphotypes, *N. incompta*, and unencrusted foraminiferal outliers. Larger points represent the spatial average of measurements across all sites, whereas smaller points represent each measurement. The average number of individuals that went into one multi-specimen measurement was 95, wherein all individuals were taken from the 150–212-µm fraction.

species, kummerforms, or other aspects of ontogeny and morphotypical variability that precluded a clear demarcation of species. For example, ambiguous *N. pachyderma* individuals included those with secondary individuals attached to the final chamber (Fig. A11), tests with extra half-chambers in the final whorl, and tests with malformed ultimate chambers. Morphotypes of *N. pachyderma* are labeled *Nps-1*, *Nps-2*, *Nps-3*, *Nps-4*, and *Nps-5* in accordance with Altuna et al. (2018). Following Altuna et al. (2018), we do not employ the distinctions "encrusted" and "nonencrusted" seen in previous work, as ultrastructure characterization is incorporated into morphotypical categorization. Deferment to morphotypical description is also more specified than "encrusted" and "nonencrusted". Below we provide a brief, colloquial synopsis of morphological traits used in the identification of the four most abundant species in conjunction with the established taxonomy of Altuna et al. (2018), Schiebel & Hemleben (2017), and Kennett & Srinivasan (1983):

- *Neogloboquadrina pachyderma* (Fig. 2.3–7) typically has four globular chambers of comparable size in the final whorl with a prominent aperture lip. However, there is significant morphotypical expression within the species. *Nps-1* has no distinct chambers in the final whorl or the spiral side. It is heavily encrusted with a pit-like umbilical aperture approximately centered on the umbilical side. On some occasions sutures may be visible on less encrusted forms. A half-chamber is sometimes present in the final whorl; it may be described as "egg-like". *Nps-2* is the typical form of *N. pachyderma*. The form appears quadrate with four chambers in the final whorl and distinct sutures. The aperture has a low arch and is confined to the width of the ultimate chamber. *Nps-3* is more rhombic in form than *Nps-2* and typically has four- and one-half chambers in the final whorl. The half-chamber is an extension of the ultimate chamber and thus creates an elongated aperture with an irregular arch. *Nps-4* has five chambers in the final whorl with a pronounced aperture lip. The aperture is typically more open than the typical form and may appear asymmetric if the last two chambers in the final whorl are fused. *Nps-5* is typically rhombic with four chambers in the final whorl and a thinner, but still pronounced, aperture lip. The slight low trochospiral form causes the aperture to open slightly toward the periphery yet remain visible from the umbilical side, resulting in a slightly asymmetrical arch and a less encrusted appearance than in other mature morphotypes.
- *Neogloboquadrina incompta* (Fig. 2.1) was identified as any test having the same morphological characteristics as *N. pachyderma* except for its dextral coiling direction (Darling et al., 2006; Schiebel & Hemleben, 2017). We note that we observed large variability in morphology amongst *N. incompta* individuals as well, but we did not discriminate between them for this study (Fig. A10).
- *Turborotalita quinqueloba* is a species often cited in marginal Arctic planktic populations (Carstens et al., 1997; Pados & Spielhagen, 2014). *Turborotalita quinqueloba* typically has five chambers in the final whorl with curved sutures and a slight positive gradation in size toward the penultimate chamber in the final whorl. The ultimate chamber is distinct from the other chambers in the final whorl because it is not globular, but rather ampullate and extended toward the aperture. The lip is pronounced, flattened, and extends over the aperture. The lip sometimes has a wavy edge. This hanging lip creates the appearance of a slit-like pseudo-aperture open toward the edge of the test. Paleo samples include spines. There are many occurrences of individuals which display some of these characteristics along with many characteristics of *N. pachyderma*. We suggest

these may be hybridized individuals. These indeterminate forms are labeled as ambiguous.

- We term a group of planktic specimens as unencrusted foraminiferal outliers (UFOs; Fig. 2.2, Fig. A9), which are characterized by their ovate ultimate chamber and arching aperture open to the edge of the test. Their ultrastructure is atypical for mature neogloboquadrinids in the Arctic Ocean and typically consists of individual conical growths of calcite with better preservation of shape and length near the aperture (Fig. 2.2, Fig. A9). Unlike mature neogloboquadrinids, calcite crystals do not typically grow together to provide uniform test coverage. Under a stereo microscope, the texture appears pearlescent rather than sugary. The final whorl typically has four to five globular chambers with straight sutures. The spiral side has defined chambers that increase in size in a low trochospiral. UFOs have thinner walls than other high latitude specimens and they typically grow to 100–200 μm.

Additionally, rare specimens of *Turborotalita humilis*, *Globigerinoides ruber*, and *Globigerina bulloides* were also identified in the assemblages. To ensure assemblage size did not impact the relative abundance of species, we duplicated three site assemblages (SWE14, PS2185, PS2170) with a difference of at least 250 individuals between replicate and original assemblages (i.e., ~300 relative to ~550 specimens). We found no significant differences between relative abundances of duplicated and original assemblages. We thus conclude that our assemblage sizes do not affect the observed relative percent abundance of species or morphotypes.

Stable Oxygen and Carbon Isotope Measurements

We measured $\delta^{18}O$ and $\delta^{13}C$ on *Nps-1*, *Nps-2*, *Nps-3*, *Nps-5*, *N. incompta*, and UFO tests, using a range of 30–80 tests from the 150–212-μm fraction for each group (Figs. 4–6). All *Nps-2* measurements were duplicated whereas other morphotype and species abundances were too low for replication. We combined analytical uncertainty and the differences between replicates (which were comparable to analytical precision) using root mean square errors. *Neogloboquadrina pachyderma-4* was excluded from geochemical analyses due to a lack of available material. For *Nps-2*, approximately 100 individual *Nps-2* tests were picked from the 150–212-μm dry fraction, gently crushed with glass plates, and homogenized using a small paintbrush. Thirty to fifty micrograms of material were partitioned for stable isotope analysis. Stable oxygen ($\delta^{18}O$) and carbon ($\delta^{13}C$) isotope values are reported in δ notation (in ‰) relative to the Vienna Pee Dee Belemnite (VPDB) scale and were measured on an instrumental setup composed of a Thermo Kiel IV Carbonate Device coupled to a Thermo Scientific MAT 253+ Mass Spectrometer housed at the Paleo^2 Laboratory at the University of Arizona. Based on repeated measurements of IAEA-603, the analytical precision over the sampling interval was 0.07‰ for $\delta^{18}O$ and 0.05‰ for $\delta^{13}C$ ($n = 15$), consistent with the long-term precision (1σ of $\delta^{18}O = 0.05$‰ & 1σ of $\delta^{13}C = 0.03$‰) of this setup.

We also collated previously published measurements of $\delta^{18}O$ and $\delta^{13}C$ on *N. pachyderma* tests from recent Arctic Ocean sediments (Fig. 6). We sub-selected only those core tops that were dated to be younger than 6 ka (Zahn et al., 1985; Poore et al., 1999; Volkmann & Mensch, 2001; Nørgaard-Pedersen et al., 2003; Hillaire-Marcel et al., 2004; Adler et al., 2009; Polyak et al., 2009; Werner et al., 2013; Xiao et al., 2014; Zehnich et al., 2020). We note that these previous studies did not differentiate between *N. pachyderma* morphotypes. The average age across the collated samples is 2.32 ka. The average age of the samples analyzed in our study is 2.8 ka.

Forward Model of *N. pachyderma* Stable Oxygen Isotopes

We compared our *N. pachyderma* $\delta^{18}O$ measurements with predicted values using oceanographic observations as input into established forward models of foraminiferal calcite $\delta^{18}O$. Temperature and salinity values across multiple depths were taken from the World Ocean Atlas (Locarnini et al., 2019; Zweng et al., 2019) and used to predict *N. pachyderma* $\delta^{18}O$ using the Bemis et al. (1998) low-light temperature equation and the LeGrande & Schmidt (2006) salinity–$\delta^{18}O_{seawater}$ equation for the Arctic Ocean:

$$T(^{\circ}C) = 16.5 - 4.8(\delta^{18}O_f - \delta^{18}O_{sw}) \quad (1)$$

$$\delta^{18}O_{sw} = 0.48(salinity) - 16.82 \quad (2)$$

where T is seawater temperature, $\delta^{18}O_f$ is foraminiferal $\delta^{18}O$, and $\delta^{18}O_{sw}$ is seawater $\delta^{18}O$.

Forward-modeled foraminiferal calcite $\delta^{18}O$ values were averaged across a one-degree square around core site coordinates prior to comparison with measured values. This combination of equations provided the most reasonable estimates of *N. pachyderma* $\delta^{18}O$ as compared to other experimental light regimes and species (not shown) presented by Bemis et al. (1998).

Mg/Ca Analysis

We measured Mg/Ca in *N. pachyderma* tests as a proxy for oceanic temperatures. For elemental measurements, we took the remnant split of the crushed *Nps-2* tests and cleaned samples following established Mg/Ca cleaning protocols (Barker et al., 2003). Prior to cleaning, crushed samples were visually inspected to ensure that non-calcareous grains were absent. The cleaning procedure we followed included clay removal using water and methanol rinses, removal of organic matter using a buffered solution of hydrogen peroxide, and ultimately, dissolving for elemental analysis following a weak nitric acid leaching step (Barker et al., 2003). We analyzed samples on a Thermo iCAP 7400 inductively coupled plasma-optical emission spectrometer housed at the Paleo^2 Laboratory at the University of Arizona. An internal gravimetric standard was employed between samples to correct for instrumental drift and to assess precision (Schrag, 1999). Repeated analysis of external matrix-matched standards using the same analytical grade nitric acid solution yielded a precision of ±0.12% ($1\sigma = 0.018$ mmol/mol).

Calculated Temperature and Seawater $\delta^{18}O$

Using the paired $\delta^{18}O$-Mg/Ca measurements on *Nps-2* specimens, we computed temperature and salinity using previously published calibration equations (Fig. 7) and obtained uncertainty estimates using the Paleo-Seawater Uncertainty Solver (PSU Solver) algorithm (Thirumalai et al., 2016). The PSU Solver allows user input of the relationships between foraminiferal $\delta^{18}O$, Mg/Ca, and temperature and $\delta^{18}O_{seawater}$, and iteratively solves for the latter two variables and their

respective uncertainties in a Monte Carlo framework (Thirumalai et al., 2016). We reconstruct seawater temperatures using the following published calibration equations, where Mg/Ca is the magnesium to calcium ratio in measured foraminiferal calcite, and T is temperature of calcification:

Plankton tows in the Fram Strait and cultured specimens from Bodega Bay, CA (Livsey et al., 2020):

$$\mathrm{Mg/Ca} = 0.93\left(e^{(0.086\mathrm{T})}\right) \quad (3)$$

Irminger Sea Sediment Trap Samples (Jonkers et al., 2013):

$$\mathrm{Mg/Ca} = 0.60\left(e^{(0.09\mathrm{T})}\right) \quad (4)$$

Core tops from the Norwegian Sea (Nürnberg et al., 1996; Kozdon et al., 2009):

$$\mathrm{Mg/Ca} = 0.13(\mathrm{T}) + 0.35 \quad (5)$$

$$\mathrm{Mg/Ca} = 0.41\left(e^{(0.083\mathrm{T})}\right) \quad (6)$$

Core tops from the Southern Ocean (Vázquez Riveiros et al., 2016):

$$\mathrm{Mg/Ca} = 0.58\left(e^{(0.084\mathrm{T})}\right) \quad (7)$$

No Mg/Ca-temperature calibrations have been developed at sites proximal to our sampling region. Furthermore, a range of non-thermal influences including salinity, bottom water calcite saturation, and pH can modulate foraminiferal Mg/Ca and thereby affect calculations of temperature (Khider et al., 2015; Gray & Evans, 2019; Tierney et al., 2019; Holland et al., 2020). However, culture and core top studies have shown that pH and/or carbonate ion concentrations and bottom water calcite saturation do not significantly affect *N. pachyderma* Mg/Ca (Davis et al., 2017; Tierney et al., 2019). Moreover, recent culture experiments indicate very low *N. pachyderma* Mg/Ca sensitivity ($\sim$0.5 mmol/mol per $>$20 salinity changes) to salinity (Bertlich et al., 2021). Equations incorporating the influence of salinity on Mg/Ca, but developed for other planktic species (Kısakürek et al., 2008; Tierney et al., 2015) yielded unrealistic temperatures for our *N. pachyderma* Mg/Ca values.

Using our paired foraminiferal δ^{18}O-Mg/Ca data at each site as input into PSU Solver, we calculated $\delta^{18}O_{seawater}$ (Eqn. 1) and salinity (Eqn. 2) and their uncertainties. We then compared the inverted temperature and salinity estimates to observations from WOA (Fig. 7). We submit that this exercise is qualitative and for illustrative purposes; as the core tops are not all modern, we caution that differences between observations and inverted values may arise due to climatic change from the age of the core top relative to present-day observations.

Additionally, we applied the 'BayFox' algorithm to our *N. pachyderma* δ^{18}O data. 'BayFox' is based on a Bayesian calibration of the δ^{18}O paleothermometer tailored to reconstruct seawater temperature from stable oxygen isotope data for planktic foraminifera (Malevich et al., 2019). We used Equation 2 to derive seawater δ^{18}O from WOA observations of salinity from 0–150 m as input into BayFox. We then used 0°C, the approximate temperature of $\sim$50–100 m depth at our sites, as the prior mean seawater temperature (Timmermans & Marshall, 2020). Finally, we use the standard deviation of WOA seasonal temperature variability at 0–150 m depth at all sites (0.34°C) as the prior on the standard deviation.

RESULTS

Mid- to Late Holocene Aged Core Tops with Minimal Post-Depositional Alteration

Radiocarbon ages confirm that all sediment samples in this study are younger than 6 ka (Fig. 6). We note that our core-top samples are, on average, younger than those used to reconstruct modern conditions using *N. pachyderma* in previous studies (Fig. 6). Of note is site B31, which is dated to 1.4 ka, exceptionally young for central Arctic Ocean sites. Our radiocarbon dates also indicate that our Eastern Siberian Shelf (ESS) sites (SWERUS 13–22) are significantly younger than our central Arctic core tops as well as Canadian and central Arctic cores from previous studies.

Ratios of benthic to planktic foraminiferal abundances are consistently low across sites (average $\simeq$11%; Fig. A5) and provide confidence for good preservation of planktic individuals. Site SWE22 has an unusually high benthic/planktic ratio (50.7%). The presence of UFOs, a thin-walled group of individuals, further suggests that samples are minimally affected by dissolution. Visual analysis of *Nps-2* indicates intact calcite preservation and minimal to no recrystallization (Fig. 2, Fig. A5). We additionally note that the average grading for post-depositional alteration at our site based on microimaging was 3.2, where 5 represents a pristine sample (see Materials and Methods). We note that site SWE18 is notable for low amounts of (thin-walled) UFOs and that this site showed the highest benthic to planktic ratio, indicating the potential for some dissolution. However, the shallow depth (349 m) of this site could have some influence on these observations. We note that other SWERUS sites do not exhibit the same high benthic-planktic ratios and show better preservation and notable percentages of UFOs.

We found no significant correlations between radiocarbon ages and *N. pachyderma* Mg/Ca or δ^{13}C across its morphotypes. Interestingly, we find significant negative relationships between δ^{18}O across all measured species and the radiocarbon age of our core tops (e.g., *Nps-2* depicted in Fig. 6), indicating that younger samples are associated with higher δ^{18}O values (i.e., consistent with cooler and/or higher $\delta^{18}O_{seawater}$/salinity conditions). Dissolution (with or without recrystallization) would serve to preferentially heighten older samples' δ^{18}O values (Lohmann, 1995)—something we do not observe. Additionally, we find weak, negative correlations between average δ^{18}O values and water depth, with shallower sites displaying higher δ^{18}O. This observation further suggests that our measurements are not affected by dissolution or recrystallization, both of which would induce anomalously positive δ^{18}O values at greater depths (Edgar et al., 2015).

Consistent Planktic Diversity across Sites

We find similar relative abundances of planktic foraminiferal species across sites (Fig. 3a). All planktic species

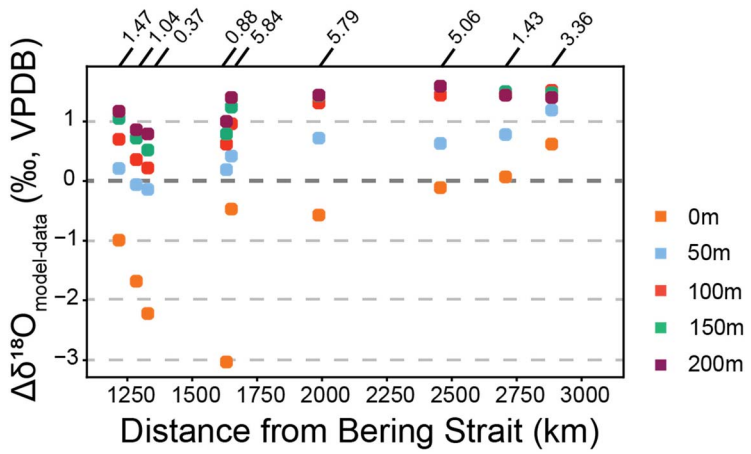

FIGURE 5. Difference between forward-modeled foraminiferal $\delta^{18}O$ using World Ocean Atlas mean annual temperature and salinity and multi-specimen *Nps-2* $\delta^{18}O$ measurements. $\Delta\delta^{18}O = 0$ represents no difference between predicted values and measured values. Data are plotted in a transect relative to site distance from the Bering Strait. Calibrated radiocarbon ages are listed above (each site in ka).

percentages are reported relative to the total number of planktic foraminifera. *Neogloboquadrina pachyderma* is the dominant species, making up at least 85% of the planktic foraminiferal population at each site and 90% on average. *Neogloboquadrina incompta* (2–7% of all planktic foraminifera, average = 5±0.01%) and UFOs (0–4% of all planktic foraminifera, average = 2±0.02%) are also significantly present at all sites, except for SWE18. *Turborotalita quinqueloba* is present at every site, however it comprises 0.2–1.4% (average = 0.6±0.00%) of all planktic foraminifera. This contrasts with previous work in the Fram Strait showing a higher prevalence of the species (Pados & Spielhagen, 2014; Schiebel et al., 2017). Benthic foraminifera make up 0–34% of our foraminiferal assemblages with an average of 8±0.12%, relative to the sum of both planktic and benthic foraminifera (Fig. A5). Ambiguous individuals are minimal and make up no more than 4% of the planktic foraminiferal population (Fig. 3).

Morphotypical variability of *N. pachyderma* was also found to be consistent across sites (Fig. 3b). The most abundant morphotype of *N. pachyderma* is *Nps-2*, making up at least 44% (average = 59±0.05%) of *N. pachyderma* at our sites. The next most abundant are *Nps-3* (10–20%, average = 15.5±0.03% of total *N. pachyderma*) and *Nps-1* (7–21%, average = 15±0.05% of total *N. pachyderma*). *Neogloboquadrina pachyderma-4* (2–6%, average = 3.7±0.02% of total *N. pachyderma*) and *Nps-5* (1–9%, average = 4.8±0.02% of total *N. pachyderma*) are both uncommon, but present. Ambiguous *N. pachyderma* specimens (see Materials & Methods) make up 0.9–6.1% of the morphotypes of *N. pachyderma* (average = 3±0.02%). We observe the same morphotypical forms defined in Altuna et al. (2018) in the *N. incompta* population, however we do not quantify the morphotypical variability.

Stable Isotopic Comparisons Between Planktic Foraminifera

We find that the average $\delta^{18}O$ and $\delta^{13}C$ of all analyzed neogloboquadrinids across sites (including four *N. pachyderma* morphotypes and *N. incompta*) are similar (Fig. 4). UFO $\delta^{18}O$ values were consistently lower at each site (Fig. 4). Inter-site averages of morphotypes *Nps-1* $\delta^{18}O$ (2.35±0.6‰), *Nps-2* $\delta^{18}O$ (2.22±0.28‰), *Nps-3* $\delta^{18}O$ (2.32±0.39‰), *Nps-5* $\delta^{18}O$ (2.07±0.45‰) were statistically indistinguishable within uncertainty relative to each other and relative to average *N. incompta* $\delta^{18}O$ (2.22±0.45‰). We found no systematic offsets between morphotypes or species within each site, as delineated by the average differences relative to *Nps-2* values, the dominant morphotype; differences between *Nps-2* and *Nps-1* (spatial average = 0.13±0.43‰), *Nps-3* (0.11±0.26‰), *Nps-5* (–0.15±0.35‰), and *N. incompta* (0.01±0.34‰) showed no consistent offsets. In contrast, average UFO $\delta^{18}O$ (1.44±0.61‰) differs significantly from *N. pachyderma* and *N. incompta*. The difference between *Nps-2* and UFO $\delta^{18}O$ (average inter-site difference = –1.1±0.87‰) is consistently negative at each site. Values of $\delta^{13}C$ for all measured *N. pachyderma* morphotypes, *N. incompta*, and UFOs are statistically indistinguishable (Fig. 4).

To obtain insights into average depths of *N. pachyderma* calcification across our samples, we compared *Nps-2* $\delta^{18}O$ with forward-modeled $\delta^{18}O$ at various depths (Fig. 5). We stress this exercise is not an ideal comparison as our core tops are not modern and four of our core tops are older than 1,500 years. Nevertheless, we find that *N. pachyderma* $\delta^{18}O$ at our youngest sites located in the Eastern Siberian Sea compare well with forward-modeled $\delta^{18}O$ using annual mean temperature and salinity observations at 50–100 m depth (Fig. 5). However, the forward model appears to overestimate measured $\delta^{18}O_{calcite}$ toward the central Arctic, where samples are, on average, older than 1.5 ka and are apparently consistent with near-surface temperature and salinity.

Our *N. pachyderma* stable isotope measurements fill in key spatial gaps for Arctic core-top studies (Fig. 6). Although our values are within the range of those from previous studies of mid- to late Holocene sediments (Fig. 6b–c; note that they did not discriminate for morphotypes), we also observe distinct differences imposed by regional Arctic oceanography. Across new and previous measurements, we find that average mid- to late Holocene foraminiferal $\delta^{18}O$ is 1.91±0.52‰ and $\delta^{13}C$ is 0.95±0.22‰ across the Arctic Ocean. Average *N. pachyderma* $\delta^{18}O$ is slightly higher in our study (average $\delta^{18}O$ = 2.09±0.24‰) than previous studies (average $\delta^{18}O$ = 1.79±0.30‰) in the central Arctic Ocean (1500–3000 km

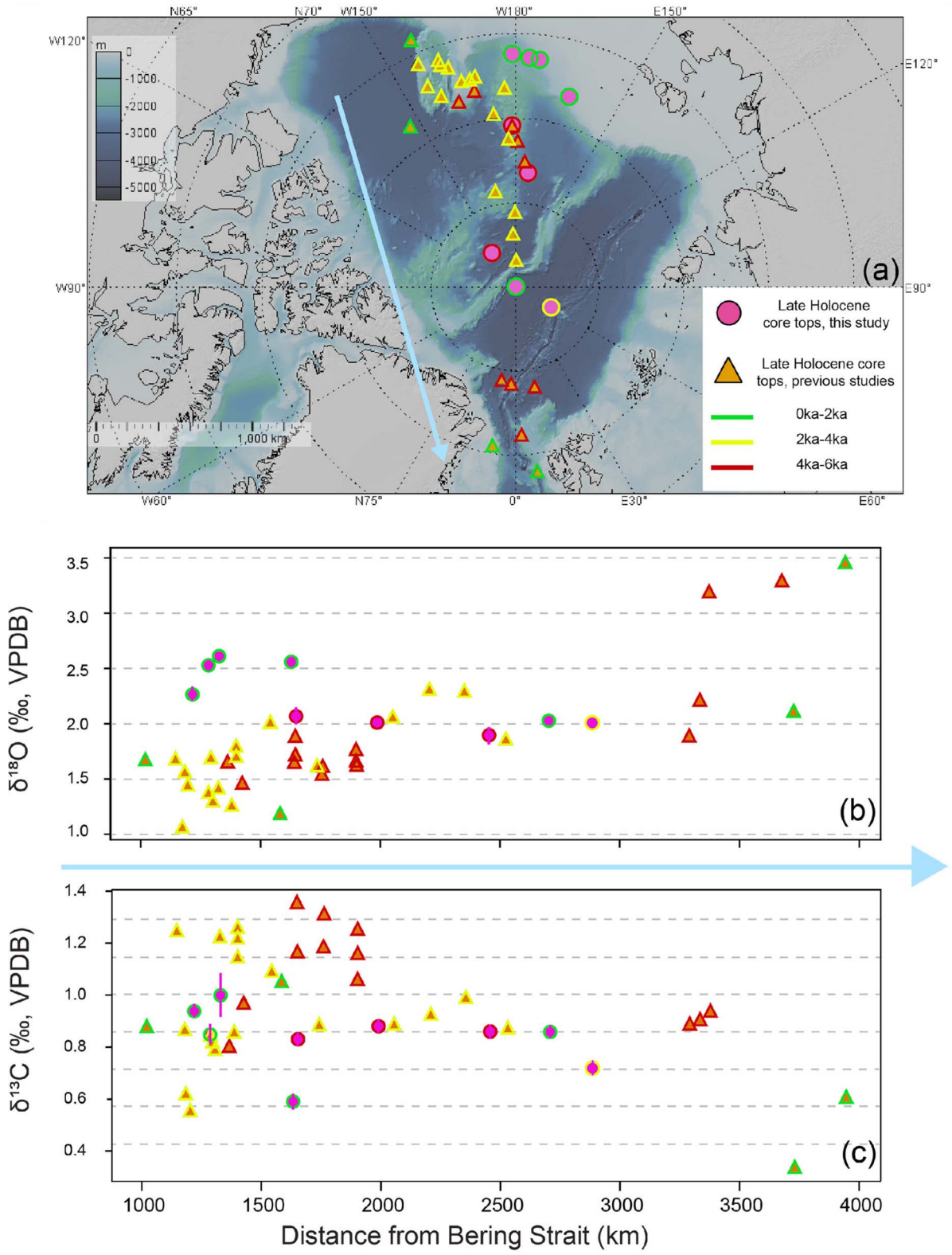

FIGURE 6. Comparison between *N. pachyderma* stable isotope measurements with previous studies. a) Bathymetry of the Arctic Ocean where sites in our study (pink circles) and previous studies (orange triangles) are depicted. Green outlines represent samples dated to 2–0 ka, yellow outlines represent samples dated between 4–2 ka, and red outlines represent samples dated between 6–4 ka. The blue arrow indicates arrangement of samples in the subsequent plots. b) Foraminiferal $\delta^{18}O$ from this study (pink) and previous studies (orange) arranged in proximity to the Bering Strait. Error bars depict root mean square errors of combined analytical and sampling uncertainty in our measurements. c) Foraminiferal $\delta^{13}C$ from this study (pink) and previous studies (orange) arranged in proximity to the Bering Strait.

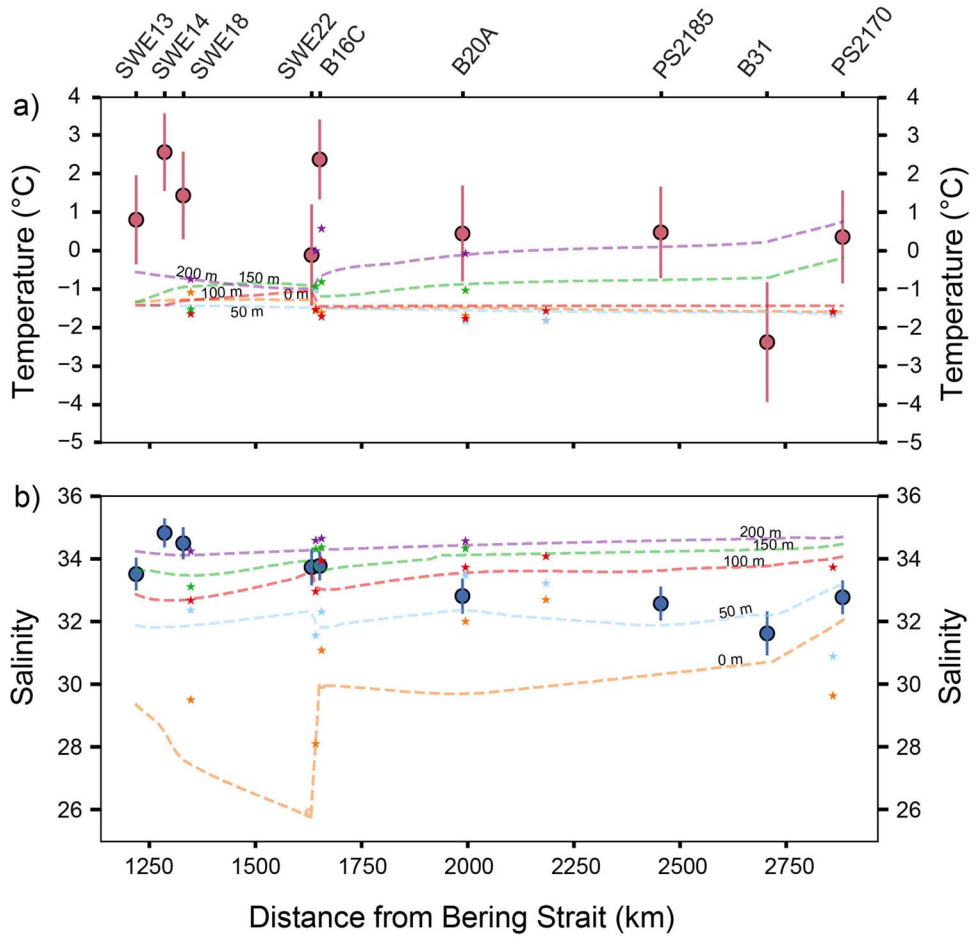

FIGURE 7. a) Seawater temperature (pink circles, left axis) at each core site (arranged in proximity to the Bering Strait) reconstructed from *Nps-2* Mg/Ca data (Eqn. 3). Dashed lines (right axis) show WOA temperature data at 0–200 m. Depths are labeled accordingly. b) Salinity (blue circles, left axis) calculated using reconstructed temperature (Eqn. 3) and *Nps-2* $\delta^{18}O$ (Eqn. 2). Dashed lines (right axis) represent WOA salinity data. Depths are labeled accordingly. Stars represent CTD observations at sites nearby our core sites; note that stars are color-coded to match depths appropriately.

from the Bering Strait). This slightly lower average is driven by low $\delta^{18}O$ values in the older cores closer to the Bering Strait (Fig. 6b). There is a clear deviation between $\delta^{18}O$ in our sites and previous work in the Pacific-adjacent region of the Arctic Ocean (Fig. 6b). Limiting the distance from the Bering Strait to 0–1600 km, *N. pachyderma* in the Eastern Siberian Sea are enriched in ^{18}O (average $\delta^{18}O = 2.47 \pm 0.18$‰) relative to samples from the Chukchi Sea region (average $\delta^{18}O = 1.56 \pm 0.24$‰). We note sites next to each other show similar isotopic values, denoting different isotopic regimes within the data. Average *N. pachyderma* $\delta^{13}C$ from this study (0.84 ± 0.12‰) is indistinguishable from $\delta^{13}C$ of previous studies within observed intersite variability (0.98 ± 0.23‰; Fig. 6). We find that spatial variations in *N. pachyderma* $\delta^{13}C$ are much smaller in magnitude across the Arctic Ocean than compared to their $\delta^{18}O$ composition (Fig. 6).

Evaluating Temperature Calibrations and $\delta^{18}O_{seawater}$ Reconstructions

We assessed the suitability of several Mg/Ca-temperature relationships for our core-top measurements of *N. pachyderma* (Table 4). Jonkers et al. (2013) developed a temperature equation using North Atlantic Ocean sediment traps over a temperature range of 5–10°C. The equations of Kozdon et al. (2009) and Nürnberg et al. (1996) were established using sub-Arctic samples from the Norwegian Sea, with temperature ranges of 3–6°C and 0–15°C, respectively. Vázquez Riveiros et al. (2016) used Southern Ocean samples to develop an equation with a temperature range of –1–9°C. Livsey et al. (2020) utilized samples from Fram Strait plankton tows and cultured specimens captured in Bodega Bay to develop a Mg/Ca-temperature equation within –2–12°C. When compared with other equations, Livsey et al. (2020)'s relationship provides the most reasonable estimates for Arctic sites relative to observed temperatures (Table 4). All other equations yield average inter-site temperatures ranging from 5–11°C—unrealistically warm for Arctic sites, across any part of the water column (Fig. 7).

We then compared the reconstructed temperatures with the temperatures observed at depth. Conductivity and temperature at depth (CTD, Fig. 7) observations were available at locations close to our core sites (Anderson, 2006; Swift, 2006; Rabe & Wisotzki, 2010; Björk, 2017). Across these sites, observed temperatures at 0 m, 50 m, 100 m, 150 m, and 200 m range from –1.80 to 1.09°C (average = -1.12 ± 0.89; Fig. 7). From 0–50 m (of these selected depths) temperatures range from –1.80 to –0.98°C (average = -1.57 ± 0.21). From

0–100 m, temperatures range from –1.49 to 1.90°C (average = –0.16±1.02). From 0–50 m, temperatures are relatively constant from site B31 to site SWE13 (from the central Arctic Ocean to the Eastern Siberian Shelf); however, at 100–200 m, temperatures slightly decrease from B31 to SWE13 and exhibit higher variability (Fig. 7). World Ocean Atlas temperatures at these sites are similar to CTD observations, but slightly underestimate temperature from 0–100 m by an average of 0.03±0.4°C. At 150–200 m, this underestimation is more noticeable (average = –0.28±1.06°C), but still less than 1°C on average. Temperatures calculated from *Nps-2* Mg/Ca using the Livsey equation are relatively warmer compared to observed temperatures, which range from –2–0.5°C in the upper 200 m of the Arctic Ocean when excluding the Fram Strait (Pnyushkov and Polyakov, 2022; Fig. 7). Nevertheless, compared to reconstructed temperatures using the Livsey et al. (2020) equation, we find that *N. pachyderma* Mg/Ca-temperatures at most sites suggest calcification at 150 m or deeper, with the East Siberian Shelf sites exhibiting the warmest reconstructed temperatures and, by extension, deepest reconstructed calcification depth (Fig. 7). At these sites, which are more recently aged (<1.5 ka) than others and likely compare better with observations, the Livsey et al. (2020) equation appears to predict temperatures that are too warm, especially considering that forward-modeled $\delta^{18}O$ predicts shallower (~50–100 m; Fig. 5, Fig. A7) apparent calcification depths.

Reconstructed $\delta^{18}O_{seawater}$ values across core tops ranged from –2 to 0‰ (VSMOW). We note that these compare well with proximal $\delta^{18}O_{seawater}$ measurements from the Laptev Sea, which range between –2.14 and 0.22‰ (VSMOW) at water depths of 40 to 200 m (Bauch & Cherniavskaia, 2018). Salinity calculated from our core-top $\delta^{18}O_{seawater}$ values (Eqn. 2) ranged from a maximum of 34.8±0.5 at site SWE14 to 31.6±0.7 at site B31 (Fig. 7). We then compared these values to WOA salinity at various depths (Fig. 7b), which showed a consistent trend of deepening toward the East Siberian Sea sites, in agreement with forward-modeled foraminiferal $\delta^{18}O$ (Fig. 5). However, we acknowledge that deeper apparent calcification depths of the East Siberian Sea according to the salinity comparison (~100–200 m; Fig. 7b) relative to forward-modeled calcite $\delta^{18}O$ (~50–100 m; Fig. 5) may arise due to uncertainty in calibrations of foraminiferal Mg/Ca composition and seawater temperature. Similar to expectations from reconstructed temperature, this exercise also suggests that *N. pachyderma* in the Eastern Siberian Sea region may calcify at deeper depths than individuals in the central Arctic (Fig. 7b). We further compared our measurements with seasonal trends in forward-modeled $\delta^{18}O$, temperature, and salinity (Figs. A7–A8) but found that seasonality amongst sites was unable to explain our observed trends.

DISCUSSION

Our work provides a mid- to late Holocene baseline of planktic foraminiferal species abundances and benthic-planktic ratios, *N. pachyderma* morphotypical abundances, $\delta^{18}O$ and $\delta^{13}C$ of multiple foraminiferal species, and *Nps-2* Mg/Ca measurements across nine East Siberian Shelf and central Arctic core tops. The youngest core top dates to 0.37 ka, five core tops are younger than 1.5 ka, and four range from 3.36 to 5.84 ka. The older core-top ages occur due to relatively low sedimentation rates and dynamic sedimentary settings across Arctic subregions (Bröder et al., 2016; Gemery et al., 2017), and are a consistent source of complexity in Arctic core-top studies (Xiao et al., 2014). Bioturbation in the Arctic Ocean is relatively low, with mixing rates ranging from ~0.27 cm/yr in deep water sites near Svalbard to ~0.04 cm/yr in the central Arctic Ocean under permanent ice (Soltwedel et al., 2019). The mid-Holocene core tops in our samples preclude quantitative comparisons of measurements with modern observations across all sites. As such, we refrain from attributing precise depths of *N. pachyderma* calcification or performing Mg/Ca-temperature calibrations and contrast all sites with observations for illustrative purposes (Figs. 5, 7). Despite the older core tops, the lack of correlation between water depth and $\delta^{18}O$, $\delta^{13}C$, and Mg/Ca, respectively; consistently low benthic-planktic ratios across samples; and microimaging analysis collectively point to the pristine nature of calcite preservation in our samples.

All sites have approximately the same distribution of planktic foraminiferal species and *N. pachyderma* morphotypes. Despite the observed surface and subsurface temperature and salinity gradients across our sites (Figs. 1, 7), we find no obvious relationships between local oceanography and relative distribution of species and *N. pachyderma* morphotypes. Although we do not observe modern spatial trends in morphotypical distribution, we do not discount *N. pachyderma* morphotypical assemblages as a tool for studying major changes in Arctic paleoceanography. Even though there are sharp changes in salinity and sea ice distributions across these sites, morphotype and species assemblages may be responding to temperature gradients, which are much smaller than salinity changes, and the average makeup of Pacific versus Atlantic waters at these sites. These oceanographic parameters might have changed significantly over the Quaternary (Poore et al., 1999), and we therefore suggest that spatially distributed downcore studies of assemblages may provide more insight into this issue. Overall, however, our measurements suggest relatively stable planktic foraminiferal species and *N. pachyderma* morphotype distributions from the Eastern Siberian Shelf to the central Arctic and provide a baseline for future downcore work.

Previous work has discounted the presence of *N. incompta* in the Arctic and surrounding areas (Altuna et al., 2018; Volkmann, 2000). However, we find that they are significantly present across our sites, exhibit the same morphotypical diversity as *N. pachyderma*, and exhibit virtually identical stable isotopic values as *Nps-2*. *Neogloboquadrina incompta* occurs more frequently than 1–3% of the planktic assemblage, indicating it is likely not a type of *N. pachyderma* (Darling et al., 2006), and is distinct at the species level; future genetic analyses can confirm or refute this hypothesis. Darling et al. (2006) also notes *N. pachyderma* is almost entirely sinistral at high latitudes (low temperatures) and shows "type *N. incompta*" plates which confirm our observations, adding further confidence to our identification. We follow convention and label all dextral neogloboquadrinids adhering to the appropriate taxonomy *N. incompta* (Darling et al., 2006; Ovechkina et al., 2010; Schiebel & Hemleben, 2017; Lam & Leckie, 2020; Brummer & Kucera, 2022). Furthermore, trends in the relative abundances of *N. incompta* and *N. pachyderma* across sites are distinct (Fig. 3). The isotopic similarity of *N. incompta* to *N. pachyderma* (Fig. 4) makes it unlikely that these specimens are present solely due to transport from the North Atlantic, as has been asserted previously by

Volkmann (2000). We also recognize previous work by Davis et al. (2020) which suggests that high stress environments may cause *N. pachyderma* to reproduce with a higher percentage of dextrally coiling offspring, although we defer to previous *in situ* observations from plankton tows supporting the findings of Darling et al. (2006) and the conclusion these are *N. incompta* rather than *N. pachyderma* (dextral). Significant changes in abundance and geochemistry of *N. incompta* should indicate dynamic changes in species' behavior relative to modern observations.

Similarly, UFOs are consistently present across our sites (Fig. 3), suggesting that the group is not transported from sub-Arctic waters and populates the Arctic Ocean. Additionally, UFO samples exhibit $\delta^{18}O$ values consistent with Arctic oceanographic conditions (Fig. 4), making it likely they are an in-situ population. Unencrusted foraminiferal outliers are the only specimens in this study that consistently show an isotopically distinct regime relative to the other species. Although they are similar to *N. pachyderma* and *N. incompta* in $\delta^{13}C$, they exhibit relatively lower $\delta^{18}O$ values. Lower $\delta^{18}O$ values suggest a warmer and/or less saline calcification environment, which is found in surface waters at our sites. This suggests that UFOs likely calcify at a shallower depth relative to *N. pachyderma* and *N. incompta*. This group is abundant enough to perform geochemical analyses, and we suggest it may be a useful species to reconstruct changes in surface-ocean mixing in the Arctic Ocean.

Unencrusted foraminiferal outliers are likely immature *N. pachyderma.* The unencrusted texture of solitary, conical calcite crystals shares some similarity with the ultrastructure of *Nps-5* in Altuna et al. (2018). However, the geometry of the test is much more planar and rhombic than the quadrate forms of mature *N. pachyderma*, and the apertures of UFOs are consistently open, ovate, lacking a distinct apertural lip, and open to the edge rather than the umbilical side (Fig. A9). We do not observe clear evidence of spines and suggest their ultrastructure does not resemble sub-Arctic or temperate species. We found several mature individuals in our samples which fit *Nps-5* morphology. When comparing stable isotopic values of UFOs and *Nps-5*, it is clear that *Nps-5* values are similar to other neogloboquadrinids, yet UFO values appear as outliers relative to the neogloboquadrinids (Fig. 4), establishing them as geochemically and morphologically distinct. Therefore, we posit UFOs are immature neogloboquadrinids with atypical morphology due to their developmental stage.

This is consistent with the lower $\delta^{18}O$ values observed in UFOs, as we would expect unencrusted, immature individuals or juveniles to calcify higher in the water column and descend as they mature (Hillaire-Marcel et al., 2004). Tell et al. (2022) also supports this understanding of *N. pachyderma* ecology and vertical migration. We note that we observe UFOs to be a similar size to mature neogloboquadrinids, which aligns with their models of a fixed depth habitat, (i.e., the relative age of the individual does not impact the preferred depth habitat, resulting in a mix of weights and sizes at all depths where individuals are observed. Additionally, it has been shown that *N. pachyderma* exhibit a large range of morphological variability during asexual reproduction, making it likely immature individuals do not conform to typical mature taxonomy (Davis et al., 2020). However, due to the taxonomic features inconsistent with typical neogloboquadrinid forms, comparable size of these specimens to some mature neogloboquadrinids, and evidence of 4–5 chambers in the final whorl, we cannot rule out the possibility of a hybrid species without further work beyond the scope of this paper. For this reason, we refrain from conclusively identifying this group in this paper.

We found near-identical $\delta^{18}O$ and $\delta^{13}C$ signatures of *N. pachyderma* morphotypes across our sites, with no evidence for systematic offsets between morphotypes (Fig. 4). In contrast, across Canadian Archipelago samples, Altuna et al. (2018) reported distinct isotopic signatures for different *N. pachyderma* morphotypes. They suggested that these differences arose due to different test sizes between morphotypes, which may be representative of different calcification parameters including depth and seasonality. This hypothesis has not yet been tested in the "open" Arctic Ocean. Our dataset suggests that morphotypes of *N. pachyderma* calcify in similar regimes across Arctic Ocean. We also find no significant differences between stable isotope values of *N. pachyderma* and *N. incompta*, indicating a shared and variable Neogloboquadrinid calcification environment across the Arctic Ocean. Therefore, we suggest the potential for bias in *N. pachyderma* geochemical studies related to morphotypes or spurious *N. incompta* individuals is minimal. Given the difficulty distinguishing between dextral kummerforms of *N. pachyderma* and true *N. incompta* and limited sample sizes in the Arctic Ocean, our results support the geochemical utility of non-selective neogloboquadrinid sampling in downcore reconstructions of Arctic paleoceanography.

Poor preservation likely does not drive the trends we observe in foraminiferal $\delta^{18}O$. Whereas the negative relationship observed between $\delta^{18}O$ and age could arise due to temporal changes between subperiods of the Holocene or due to spatial differences in average hydrographic conditions across sites, we note that dissolution and recrystallization would induce the opposite trend—older samples would have more positive $\delta^{18}O$ values (Edgar et al., 2015). Previous work using biomarkers and ostracode assemblages have shown cooling starting from 7 ka (Duplessy et al., 2001; Fahl & Stein, 2012; Gemery et al., 2017). While the amount of perennial ice likely increased between the mid-Holocene and present, paleorecords show relatively stable sea ice conditions in the central Arctic since 6 ka analogous to modern observations (Fahl & Stein, 2012; Gemery et al., 2017). Thus, we caution that the overestimation of observations by forward-modeled calcite $\delta^{18}O$ in the central Arctic (Fig. 5) may arise spuriously due to older samples capturing mid-Holocene hydrographic conditions. Yet we note that sample B31, which is located proximal to the North Pole, dates to 1.43 ka and also exhibits consistency with a shallower depth according to forward-modeled $\delta^{18}O$. Alternatively, if these values are representative of mean-state conditions across the mid- to late Holocene, this trend would still be consistent with deeper calcification in the younger Eastern Siberian Sea samples relative to a shallower *N. pachyderma* calcification depth in the central Arctic. The more marginal samples we analyze are young and do not pose the same temporal problems. Therefore, we suggest that our geochemical measurements reflect in-situ calcification values that capture mean conditions of the mid- to late Holocene and are minimally impacted by dissolution or post-depositional alteration.

TABLE 2. *Neogloboquadrina pachyderma*, *N. incompta*, and unencrusted foraminiferal outlier $\delta^{18}O$ and $\delta^{13}C$ values for each core site reported in ‰ relative to VPDB.

Lab ID	*Nps-1* $\delta^{18}O$	*Nps-1* $\delta^{13}C$	*Nps-2* $\delta^{18}O$	*Nps-2* $\delta^{13}C$	*Nps-3* $\delta^{18}O$	*Nps-3* $\delta^{13}C$	*Nps-5* $\delta^{18}O$	*Nps-5* $\delta^{13}C$	*N. incompta* $\delta^{18}O$	*N. incompta* $\delta^{13}C$	UFO $\delta^{18}O$	UFO $\delta^{13}C$
SWE13	2.53	0.96	2.27	0.94	2.33	0.93	2.24	0.75	2.29	0.95	1.49	0.99
SWE14	2.87	0.80	2.53	0.85	2.56	0.98	2.15	0.85	2.53	0.90	1.69	0.91
SWE18	3.01	0.66	2.61	1.00	2.74	0.86	2.61	0.76	2.55	0.81	n/a	n/a
SWE22	3.02	0.77	2.56	0.59	2.86	0.79	2.37	0.63	2.75	0.75	1.79	0.79
B16C	1.55	0.67	2.07	0.83	1.81	0.96	1.15	0.76	1.37	0.95	0.40	1.20
B20A	1.79	0.81	2.01	0.88	1.86	0.91	1.66	0.80	1.71	0.85	1.29	1.04
PS2185	2.40	0.68	1.89	0.86	2.16	0.86	1.88	0.83	2.35	0.74	1.09	0.81
B31	1.50	1.12	2.03	0.86	1.98	0.88	2.41	0.68	2.15	0.90	n/a	n/a
PS2170	2.47	0.73	2.01	0.72	2.61	0.90	2.18	0.80	2.33	0.72	2.33	0.70
Average	2.35	0.80	2.22	0.84	2.32	0.90	2.07	0.76	2.22	0.84	1.44	0.92
Standard Deviation	0.60	0.15	0.28	0.12	0.39	0.06	0.45	0.07	0.43	0.09	0.61	0.17

Local oceanographic and bathymetric settings likely drive *N. pachyderma* $\delta^{18}O$ differences between our measurements and previous studies. This separation is not driven by geological age. In the Chukchi Sea, core tops dated at 2–0 ka are isotopically consistent with older samples (Fig. 6). Comparison of values between the youngest cores across the Chukchi Sea and Eastern Siberian Shelf show the same difference. Eastern Siberian Shelf sites are on average deeper than sites in the Chukchi Sea (Fig. 6). The surface water of the Eastern Siberian Shelf primarily consists of meltwater and river runoff with variable temperatures in summer and high salinity, colder waters in winter due to sea ice formation (Wang et al., 2021). Eastern Siberian Shelf mixed layer water (0–50 m) ranges from –1.7–3.0°C and <28–31 and halocline waters range from –1.7–1.4°C and 29–34 (Wang et al., 2021). The Chukchi Sea mixed layer (0–20 m, 0–6°C and 29–32) and the halocline (–2–0°C and 32–35) are both comparable to the East Siberian Shelf (Clement Kinney et al., 2022). However, the available sites in the Chukchi Sea are closer to the Beaufort Sea and therefore the Beaufort Gyre, which is associated with the multidecadal storage of freshwater sourced from sea ice melt and freshwater influx from North American rivers (Proshutinsky et al., 2019). This creates a strong salinity gradient in the upper water column with more saline conditions in the Siberian Arctic and less saline conditions in the Canadian Arctic. In addition to the oceanographic data, the relatively higher Eastern Siberian Shelf *Nps-2* $\delta^{18}O$ suggests a cooler and more saline environment than *N. pachyderma* in the Chukchi Sea samples. Considering that these comparisons are consistent even among younger sites, we maintain that the ~1‰ difference between the Chukchi and Eastern Siberian seas accurately reflects spatial differences in regional oceanography.

Our measurements are consistent with previous studies that have demonstrated variable *N. pachyderma* calcification depths from 50–200 m across Arctic sub-regions (Bauch et al., 1997; Volkmann & Mensch, 2001; Simstich et al., 2003; Greco et al., 2019; Charette et al., 2020; Jonkers et al., 2022; Tell et al., 2022). Comparisons with seasonal observations suggest that *N. pachyderma* variably calcify over these depths regardless of season (Figs. A7–A8). Surface dwelling *N. pachyderma* $\delta^{18}O$ from plankton tows in the outer Laptev Sea range from 1–2‰ whereas subsurface *N. pachyderma* $\delta^{18}O$ range from 2–3.5‰ (Volkmann & Mensch, 2001). Tows from the Nansen Basin additionally show variable *N. pachyderma* standing stock and abundances across 0–200 m depths, with a preference for shallower calcification habitats in the interior Arctic, away from the Fram Strait (Bauch et al., 1997). Simstich et al. (2003) showed *N. pachyderma* in the Eastern Greenland Current followed isohalines of 34–35, similar to our observations (Fig. 7). Recently, Greco et al. (2019) hypothesized using plankton tows that sea ice cover influences *N. pachyderma* depth habitat, with regions of more perennial sea ice associated with shallower calcification habitats and vice-versa (Greco et al., 2019). They further posited that this shoaling underneath sea ice may be related to light availability and average water column productivity (Greco et al., 2019). Previous measurements of *N. pachyderma* $\delta^{18}O$ in Arctic surface sediments (Fig. 6) also suggest variable calcification depths (Xiao et al., 2014); however, these studies did not measure paired Mg/Ca-$\delta^{18}O$, which can lead to uncertainty related to the relative influences of $\delta^{18}O_{seawater}$ and temperature on calcite $\delta^{18}O$. Our paired $\delta^{18}O$-Mg/Ca measurements on *N. pachyderma* provide new insights into *N. pachyderma* calcification.

At the youngest sites in the Eastern Siberian Shelf (ESS), we find relatively elevated $\delta^{18}O$ (Tables 2, 3; Fig. 6b), Mg/Ca-temperature reconstructions (Table 4; Fig. 7a), and reconstructed salinity (Fig. 7b), consistent with calcification at subsurface depths composed of relatively warm and salty waters. In the ESS, sea ice cover is lower than in the central Arctic (Fig. 1c). Inferred calcification depths at these younger ESS sites differ between $\delta^{18}O$ (50–100 m; Fig. 5), temperature (>200 m; Fig. 7a), and salinity (100–150 m; Fig. 7b). While we recognize modeled $\delta^{18}O_{calcite}$ at 0 m in the ESS is driven by freshwater input from Siberia, our results suggest it is unlikely that *N. pachyderma* calcifies within the freshwater-dominated uppermost layers (Figs. 5–7). The development of local Mg/Ca-temperature calibrations

TABLE 3. Mg/Ca measurements on bulk *Nps-2* reported with *Nps-2* $\delta^{18}O$.

Lab ID	Mg/Ca (mmol/mol)	*Nps-2* $\delta^{18}O$
SWE13	1.00	2.27
SWE14	1.16	2.53
SWE18	1.05	2.61
SWE22	0.92	2.56
B16C	1.14	2.07
B20A	0.97	2.01
PS2185	0.97	1.89
B31	0.76	2.03
PS2170	0.96	2.01

TABLE 4. Temperature reconstructions from Mg/Ca measurements. All values are in °C.

Lab ID	Livsey et al. (2020)	Kozdon et al. (2009)	Jonkers et al. (2013)	Nürnberg et al. (1996)	Vázquez Riveiros et al. (2016)
SWE13	0.48	4.76	5.33	10.36	6.11
SWE14	0.45	4.74	5.3	10.33	6.08
SWE18	−2.38	3.14	2.59	7.4	3.18
SWE22	0.81	4.98	5.65	10.71	6.45
B16C	2.38	6.08	7.14	112.33	8.05
B20A	1.44	5.41	6.25	11.36	7.1
PS2185	0.36	4.69	5.21	10.24	5.99
B31	−0.11	4.4	4.77	9.76	5.51
PS2170	2.57	6.23	7.33	12.53	8.26
Average	0.67	4.94	5.51	10.56	6.3
Standard Deviation	1.47	0.93	1.4	1.52	1.5

will lead to more accurate evaluations of *N. pachyderma* calcification depths in the ESS. On the other hand, our measurements toward the central Arctic, where sea ice is more perennial than in the ESS, are consistent with a shallower *N. pachyderma* depth habitat, in line with Greco et al. (2019). Although these samples are older than the ESS samples toward the coast, similar results (and cooler temperatures) at the relatively recent site B31 proximal to the North Pole support a shallower *N. pachyderma* calcification habitat (0–50 m) in the central Arctic.

In general, marginal Arctic sites exhibit higher Mg/Ca values than at central Arctic locations. We note that the lowest value occurs at site B31 (the geographic North Pole; Table 3). However, two sites do not adhere to this overall trend. SWE22 samples have relatively low Mg/Ca compared to the other SWERUS site samples, and B16C samples display higher values relative to the more central Arctic sites. B16C Mg/Ca could be an anomalous value due to its age, as we would expect anomalously high Mg/Ca in the mid-Holocene relative to modern conditions (McKay et al., 2018). Alternatively, relatively higher Mg/Ca at this site could also arise due to the site's proximity to sea ice, which creates a much larger range of potential Mg/Ca values for lower temperatures (Vázquez Riveiros et al., 2016). Sea ice melt increases total alkalinity in the surface ocean (Lebrato et al., 2020) which could in turn lead to lower Mg/Ca in both seawater and foraminiferal calcite (Vázquez Riveiros et al., 2016), causing sites with a higher coverage of sea ice (Fig. 1c) to exhibit lower Mg/Ca relative to B16C. Regardless of the exact mechanism, our Mg/Ca values are consistent with measurements (ranging ∼0.5–1.4 mmol/mol) in the Southern Ocean (Vázquez Riveiros et al., 2016). Therefore, it is most likely our measured Mg/Ca accurately reflects seawater conditions at the time of *N. pachyderma* growth; however, the available (non-local) calibrations cannot accurately capture the empirical relationship between foraminiferal Mg/Ca and seawater temperature in the Arctic.

SUMMARY AND CONCLUSIONS

Neogloboquadrina pachyderma is the dominant species of planktic foraminifera observed in the Arctic Ocean core tops we investigated. *Neogloboquadrina incompta* was the second most abundant species at our sites. Morphotypes of *N. pachyderma* and *N. incompta* appear to calcify in the same local conditions, while unencrusted foraminiferal outliers (which we believe are predominantly immature *N. pachyderma* individuals) likely calcify in shallower waters. The stable isotopic overlap of *N. pachyderma* morphotypes points to a similar calcification environment over the mid- to late Holocene. Consistent with previous work, we find, via paired δ^{18}O-Mg/Ca measurements on *N. pachyderma*, that this species does not calcify at a singular static depth in the Arctic and instead calcifies at approximately 50–150 m. We find that some Mg/Ca-temperature relationships are more suitable than others for *N. pachyderma* in our samples and stress the need for more Arctic-specific calibrations. Our data are consistent with the hypothesis that *N. pachyderma* calcification depth shoals from the continental shelf toward the central Arctic. This pattern coincides with increasing sea ice coverage as well as increasing upper-layer salinity. Relative species and morphotype abundances as well as planktic foraminiferal geochemical measurements presented here should provide a mid- to late Holocene baseline for future investigations of Quaternary climate change in the Arctic Ocean.

ACKNOWLEDGMENTS

We thank Dr. Zachary Michaels for his assistance with imaging samples and acknowledge the help from Dr. Lael Vetter as well as other members of the University of Arizona Paleo^2 Laboratory. This work was completed with partial funding from the Cushman Foundation; we thank the foundation for their support. We would also like to thank Dr. Jessica Tierney and Dr. Diane Thompson for their feedback and input on this publication. KT acknowledges the University of Arizona Technology and Research Initiative Fund (TRIF) for support, and NSF OCE #1903482, which partially funded this work. Thomas Cronin and Laura Gemery are funded by the U.S. Geological Survey, Climate Research and Development Program and supported by the U.S.G.S. Land Change Program. Any use of trade, firm, or product names is for descriptive purposes only and does not imply endorsement by the U.S. Government. The Appendix with Table A1 and Figures A1-A11 can be found linked to the online version of this article.

REFERENCES

Aagaard, K., Grantz, A., Carmack, E., and the 1994 Arctic Ocean Section scientific party, 1996, The 1994 Arctic Ocean Section: The first major scientific crossing of the Arctic Ocean: Tucker, W., and Cate, D., (eds.), special report 96-23, US army Cold Regions Research and Engineering Laboratory, Hanover, 129 p.

Adler, R. E., Polyak, L., Ortiz, J. D., Kaufman, D. S., Channell, J. E., Xuan, C., Grottoli, A. G., and Sellen Crawford, K. A., 2009, Sediment record from the western Arctic Ocean with an improved Late Quaternary age

resolution: HOTRAX core HLY0503-8JPC, Mendeleev Ridge: Global and Planetary Change, v. 68, p. 18–29. DOI: 10.1016/j.gloplacha.2009.03.026.

Altuna, N. E. B., Pieńkowski, A. J., Eynaud, F., and Thiessen, R., 2018, The morphotypes of *Neogloboquadrina pachyderma*: Isotopic signature and distribution patterns in the Canadian Arctic Archipelago and adjacent regions: Marine Micropaleontology, v. 142, p. 13–24. DOI: 10.1016/j.marmicro.2018.05.004.

Anderson, L. G., 2006, Hydrochemistry measured on water bottle samples during ODEN cruise Beringia III, 77DN2005-08): PANGAEA. DOI: 10.1594/PANGAEA.451773.

Barker, S., Greaves, M., and Elderfield, H., 2003, September, A study of cleaning procedures used for foraminiferal Mg/Ca paleothermometry: Geochemistry, Geophysics, Geosystems, v. 4. DOI: 10.1029/2003gc000559.

Bauch, D., and Cherniavskaia, E., 2018, Water mass classification on a highly variable Arctic shelf region: Origin of Laptev sea water masses and implications for the nutrient budget: Journal of Geophysical Research: Oceans, v. 123, p. 1896–1906. DOI: 10.1002/2017JC013524.

Bauch, D., Carstens, J., and Wefer, G., 1997, Oxygen isotope composition of living *Neogloboquadrina pachyderma* (sin.) in the Arctic Ocean: Earth and Planetary Science Letters, v. 146, p. 47–58. DOI: 10.1016/s0012-821x(96)00211-7.

Bemis, B. E., Spero, H. J., Bijma, J., and Lea, D. W., 1998, Reevaluation of the oxygen isotopic composition of planktonic foraminifera: Experimental results and revised paleotemperature equations: Paleoceanography, v. 13, p. 150–160. DOI: 10.1029/98pa00070.

Bertlich, J., Gussone, N., Berndt, J., Arlinghaus, H. F., and Dieckmann, G. S., 2021, Salinity effects on cultured *Neogloboquadrina pachyderma* (sinistral) from high latitudes: New paleoenvironmental insights: GeoMarine Letters, v. 41, p. 2. DOI: 10.1007/s00367-020-00677-1.

Björk, G., 2017, CTD data from the SWERUS-C3 expedition 2014 in the Arctic Ocean. DOI: 10.1594/PANGAEA.884144, Supplement to: Björk, G., et al., 2018, Bathymetry and oceanic flow structure at two deep passages crossing the Lomonosov Ridge: Ocean Science, v. 14, p.1–13, DOI: 10.5194/os-14-1-2018.

Bond, G., Kromer, B., Beer, J., Muscheler, R., Evans, M., Showers, W., Hoffmann, S., Lotti-Bond, R., Hajdas, I., and Bonani, G., 2001, Persistent solar influence on North Atlantic climate during the Holocene: Science, v. 294, p. 2130–2136. DOI: 10.1126/science.1065680.

Brady, H. B., 1884, Report on the Foraminifera dredged by H.M.S. Challenger, during the years 1873-1876: Zoology, v. 9, p. 1–814.

Briner, J. P., Cuzzone, J. K., Badgeley, J. A., Young, N. E., Steig, E. J., Morlighem, M., Schlegel, N., Hakim, J. H., Schafer, J. M., Johnson, J. V., Lesnek, A. J., Thomas, E. K., Allan, E., Bennike, O., Cluett, A. A., Csatho, B., de Vernal, A., Downs, J., Larour, E., and Nowicki, S., 2020, Rate of mass loss from the Greenland Ice Sheet will exceed Holocene values this century: Nature, v. 586, p. 70–74. DOI: 10.1038/s41586-020-2742-6.

Bröder, L., Tesi, T., Salvado, J. A., Semiletov, I. P., Dudarev, O. V., and Gustafsson, O., 2016, Fate of terrigenous organic matter across the Laptev Sea from the mouth of the Lena River to the deep sea of the Arctic interior: Biogeosciences, v. 13, p. 5003–5019. DOI: 10.5194/bg-13-5003-2016.

Brummer, G. A., and Kucera, M., 2022, Taxonomic review of living planktonic foraminifera: Journal of Micropalaeontology, v. 41, p. 29–74. DOI: 10.5194/jm-41-29-2022.

Carstens, J., Hebbeln, D., and Wefer, G., 1997, Distribution of planktic foraminifera at the ice margin in the Arctic, Fram Strait: Marine Micropaleontology, v. 29, p. 257–269. DOI: 10.1016/S0377-8398(96)00014-X.

Cavalieri, D. J., and Parkinson, C. L., 2012, Arctic sea ice variability and trends, 1979–2010: Cryosphere, v. 6, p. 881–889. DOI: 10.5194/tc-6-881-2012.

Charette, M. A., Kipp, L. E., Jensen, L. T., Dabrowski, J. S., Whitmore, L. M., Fitzsimmons, J. N., Williford, T., Ulfsbo, A., Jones, E., Bundy, R. M., Vivancos, S. M., Pahnke, K., John, S. G., Xiang, Y., Hatta, M., Petrova, M. V., Heimburger-Boavida, L. E., Bauch, D., Newton, R., Pasqualini, A., Agather, A. M., Amon, R. M. W., Anderson, R. F., Andersson, P. S., Benner, R., Bowman, K. L., Edwards, R. L., Gdaniec, S., Gerringa, L. J. A., Gonzalez, A. G., Granskog, M., Haley, B., Hammerschmidt, C. R., Hansell, D. A., Henderson, P. B., Kadko, D. C., Kaiser, K., Laan, P., Lam, P. J., Lamborg, C. H., Levier, M., Li, X., Margolin, A. R., Measures, C., Middag, R., Millero, F. J., Moore, W. S., Paffrath, R., Planquette, H., Rabe, B., Reader, H., Rember, R., Rijkenberg, M. J. A., Roy-Barman, M., Rutgers van der Loeff, M., Saito, M., Schauer, U., Schlosser, P., Sherrell, R. M., Shiller, A. M., Slagter, H., Sonke, J. E., Stedmon, C., Woosley, R. J., Valk, O., van Ooijen, J., and Zhang, R., 2020, The Transpolar Drift as a Source of Riverine and Shelf-Derived Trace Elements to the Central Arctic Ocean: Journal of Geophysical Research: Oceans, v. 125. DOI: 10.1029/2019JC015920.

Clement Kinney, J., Assmann, K. M., Maslowski, W., Björk, G., Jakobsson, M., Jutterström, S., Lee, Y. J., Osinski, R., Semiletov, I., Ulfsbo, A., Wåhlström, I., and Anderson, L. G., 2022, On the circulation, water mass distribution, and nutrient concentrations of the western Chukchi Sea: Ocean Science, v. 18, p. 29–49. DOI: 10.5194/os-18-29-2022.

Consolaro, C., Rasmussen, T. L., Panieri, G., Mienert, J., Bünz, S., and Sztybor, K., 2015, Carbon isotope ($\delta^{13}C$) excursions suggest times of major methane release during the last 14 kyr in Fram Strait, the deep-water gateway to the Arctic: Climate of the Past, v. 11, p. 669–685. DOI: 10.5194/cp-11-669-2015.

Cronin, T., DeNinno, L., Polyak, L., Caverly, E., Poore, R., Brenner, A., Rodriguez-Lazaro, J., and Marzen, R., 2014, Quaternary ostracode and foraminiferal biostratigraphy and paleoceanography in the western Arctic Ocean: Marine Micropaleontology, v. 111, p. 118–133. DOI: 10.1016/j.marmicro.2014.05.001.

Darling, K. F., Kucera, M., Kroon, D., and Wade, C. M., 2006, A resolution for the coiling direction paradox in *Neogloboquadrina pachyderma*: Paleoceanography, v. 21. DOI: 10.1029/2005pa001189.

Davis, C. V., Fehrenbacher, J. S., Hill, T. M., Russell, A. D., and Spero, H. J., 2017, Relationships between temperature, pH, and crusting on Mg/Ca ratios in laboratory grown *Neogloboquadrina pachyderma*: Paleoceanography, v. 32, p. 1137–1152. DOI: 10.1002/2017PA003111.

Davis, C. V., Livsey, C. M., Palmer, H. M., Hull, P. M., Thomas, E., Hill, T. M., and Benitez-Nelson, C. R., 2020, Extensive morphological variability in asexually produced planktic foraminifera: Science Advances, v. 6. DOI: 10.1126/sciadv.abb89.

Duplessy, J.-C., Ivanova, E., Murdmaa, I., Paterne, M., and Labeyrie, L., 2001, Holocene paleoceanography of the northern Barents Sea and variations of the northward heat transport by the Atlantic Ocean: Boreas, v. 30, p. 2–16. DOI: 10.1111/j.1502-3885.2001.tb00984.x.

Edgar, K. M., Anagnostou, E., Pearson, P. N., and Foster, G. L., 2015, Assessing the impact of diagenesis on δ11B, δ13C, δ18O, Sr/Ca and B/Ca values in fossil planktic foraminiferal calcite: Geochimia et Cosmochimia Acta, v. 166, p. 189–209. DOI: 10.1016/j.gca.2015.06.018.

Ehrenberg, C. G., 1862, Elemente des tiefen Meeresgrundes in Mexikanischen Golfstrome bei Florida: Ober die Tiefgrund-Verhaltnisse des Oceans am Eingange der Davisstrasse und bei Island: Monatsberichte der Koniglichen Preussische Akademie der Wissenschaften zu Berlin, p. 275–315.

Ekwurzel, B., Schlosser, P., Mortlock, R. A., Fairbanks, R. G., and Swift, J. H., 2001, River runoff, sea ice meltwater, and Pacific water distribution and mean residence times in the Arctic Ocean: Journal of Geophysical Research, v. 106, p. 9075–9092. DOI: 10.1029/1999JC000024.

Fahl, K., and Stein, R., 2012, Modern seasonal variability and deglacial/Holocene change of central Arctic Ocean sea-ice cover: New insights from biomarker proxy records: Earth and Planetary Science Letters, v. 351–352, p. 123–133. DOI: 10.1016/j.epsl.2012.07.009.

Gemery, L., Cronin, T. M., Poirier, R. K., Pearce, C., Barrientos, N., O'Regan, M., Johansson, C., Koshurnikov, A., and Jakobsson, M., 2017, Central Arctic Ocean paleoceanography from ~50 ka to present, on the basis of ostracode faunal assemblages from the SWERUS 2014 expedition: Climate of the Past, v. 13, p. 1473–1489. DOI: 10.5194/cp-13-1473-2017.

Gray, W. R., and Evans, D., 2019, Influences on Mg/Ca in planktonic foraminifera: A review of culture studies and application to the Last Glacial Maximum: Paleoceanography and Paleoclimatology, v. 34, p. 306–315. DOI: 10.1029/2018PA003517.

Greco, M., Jonkers, L., Kretschmer, K., Bijma, J., and Kucera, M., 2019, Depth habitat of the planktonic foraminifera and *Neogloboquadrina pachyderma* in the northern high latitudes explained by sea-ice and chlorophyll concentrations: Biogeosciences, v. 16, p. 3425–3437. DOI: 10.5194/bg-16-3425-2019.

Greco, M., Morard, R., and Kucera, M., 2021, Single-cell metabarcoding reveals biotic interactions of the Arctic calcifier *Neogloboquadrina pachyderma* with the eukaryotic pelagic community: Journal of Plankton Research, v. 43, p. 113–125. DOI: 10.1093/plankt/fbab015.

He, F., and Clark, P. U., 2022, Freshwater forcing of the Atlantic Meridional Overturning Circulation revisited: Nature Climate Change, v. 12, p. 449–454. DOI: 10.1038/s41558-022-01328-2.

Heaton, T. J., Köhler, P., Butzin, M., Bard, E., Reimer, R. W., Austin, W. E. N., Ramsey, C. B., Grootes, P. M., Hughen, K. A., Kromer, B., Reimer, P. J., Adkins, J., Burke, A., Cook, M. S., Olsen, J., and Skinner, L. C., 2020, Marine20—the marine radiocarbon age calibration curve (0–55,000 cal BP): Radiocarbon, v. 62, p. 779–820. DOI: 10.1017/RDC.2020.68.

Hilbrecht, H., 1996, Extant planktic foraminifera and the physical environment in the Atlantic and Indian Oceans: Mitteilungen aus dem Geologischen Institut der Eidgen, Technischen Hochschule und der Universität Zürich, Neue Folge, No. 300, Zürich, 93 p.

Hillaire-Marcel, C., de Vernal, A., Polyak, L., and Darby, D., 2004, Size-dependent isotopic composition of planktic foraminifers from Chukchi Sea vs. NW Atlantic sediments—implications for the Holocene paleoceanography of the western Arctic: Quaternary Science Reviews, v. 23, p. 245–260. DOI: 10.1016/j.quascirev.2003.08.006.

Holland, M. M., and Bitz, C. M., 2003, Polar amplification of climate change in coupled models: Climate Dynamics, v. 21, p. 221–232. DOI: 10.1007/s00382-003-0332-6.

Holland, K., Branson, O., Haynes, L. L., Hönisch, B., Allen, K. A., Russell, A. D., Fehrenbacher, J. S., Spero, H. J., and Eggins, S. M., 2020, Constraining multiple controls on planktic foraminifera Mg/Ca: Geochimica et Cosmochimica Acta, v. 273, p. 116–136. DOI: 10.1016/j.gca.2020.01.015.

Jonkers, L., Brummer, G.-J. A., Meilland, J., Groeneveld, J., and Kucera, M., 2022, Variability in *Neogloboquadrina pachyderma* stable isotope ratios from isothermal conditions: Implications for individual foraminifera analysis: Climate of the Past, v. 18, p. 89–101. DOI: 10.5194/cp-18-89-2022.

Jonkers, L., Jiménez-Amat, P., Mortyn, P. G., and Brummer, G.-J. A., 2013, Seasonal Mg/Ca variability of *N. pachyderma* (s.) and *G. bulloides*: Implications for seawater temperature reconstruction: Earth and Planetary Science Letters, v. 376, p. 137–144. DOI: 10.1016/j.epsl.2013.06.019.

Kennett, J., and Srinivasan, M., 1983, Neogene Planktonic Foraminifera: A Phylogenetic Atlas: Hutchinson Ross, New York, 265 p. ISBN: 9780879330705.

Khider, D., Huerta, G., Jackson, C., Stott, L. D., and Emile-Geay, J., 2015, A Bayesian, multivariate calibration for *Globigerinoides ruber* Mg/Ca: Geochemistry, Geophysics, Geosystems, v. 16, p. 2916–2932. DOI: 10.1002/2015GC005844.

Kısakürek, B., Eisenhauer, A., Böhm, F., Garbe-Schönberg, D., and Erez, J., 2008, Controls on shell Mg/Ca and Sr/Ca in cultured planktonic foraminiferan, *Globigerinoides ruber*, white: Earth and Planetary Science Letters, v. 273, p. 260–269. DOI: 10.1016/j.epsl.2008.06.026.

Kohfeld, K. E., Fairbanks, R. G., Smith, S. L., and Walsh, I. D., 1996, *Neogloboquadrina pachyderma* (sinistral coiling) as paleoceanographic tracers in polar oceans: Evidence from northeast water polynya plankton tows, sediment traps, and surface sediments: Paleoceanography, v. 11, p. 679–699. DOI: 10.1029/96pa02617.

Kozdon, R., Eisenhauer, A., Weinelt, M., Meland, M. Y., and Nürnberg, D., 2009, Mg/Ca temperature calibrations of *Neogloboquadrina pachyderma* (sinistral) using paired δ44/40 Ca and Mg/Ca measurements: δ44/40 Ca: Geochemistry, Geophysics, Geosystems, v. 10. DOI: 10.1029/2008gc002169.

Lam, A. R., and Leckie, R. M., 2020, Late Neogene and Quaternary diversity and taxonomy of subtropical to temperate planktic foraminifera across the Kuroshio Current Extension, northwest Pacific Ocean: Micropaleontology, v. 66, p. 177–268. DOI: 10.47894/mpal.66.3.01.

Lebrato, M., Garbe-Schönberg, D., Müller, M. N., Blanco-Ameijeiras, S., Feely, R. A., Lorenzoni, L., Molinero, J., Bremer, K., Jones, D. O. B., Iglesias-Rodriguez, D., Greeley, D., Lamare, M. D., Paulmier, A., Graco, M., Cartes, J., Barcelos e Ramos, J., de Lara, A., Sanchez-Leal, R., Jimenez, P., Paparazzo, F. E., Hartman, S. E., Westernströer, U., Küter, M., Benavides, R., da Silva, A. F., Bell, S., Payne, C., Olafsdottir, S., Robinson, K., Jantunen, L. M., Korablev, A., Webster, R. J., Jones, E. M., Gilg, O., du Bois, P.B., Beldowski, J., Ashjian, C., Yahia, N. D., Twining, B., Chen, X., Tseng, L., Hwang, J., Dahms, H., and Oschiles, A., 2020, Global variability in seawater Mg:Ca and Sr:Ca ratios in the modern ocean: Proceedings of the National Academy of Sciences, v. 117, p. 22281–22292. DOI: 10.1073/pnas.1918943117.

LeGrande, A. N., and Schmidt, G. A., 2006, Global gridded data set of the oxygen isotopic composition in seawater: Geophysical Research Letters, v. 33. DOI: 10.1029/2006gl026011.

Livsey, C. M., Kozdon, R., Bauch, D., Brummer, G.-J. A., Jonkers, L., Orland, I., Hill, T. M., and Spero, H. J., 2020, High-Resolution Mg/Ca and $\delta^{18}O$ Patterns in Modern *Neogloboquadrina pachyderma* From the Fram Strait and Irminger Sea: Paleoceanography and Paleoclimatology, v. 35. DOI: 10.1029/2020PA003969.

Locarnini, M., Mishonov, A., Baranova, O., Boyer, T., Zweng, M., Garcia, H., Reagan, J., Seidov, D., Weathers, K., Paver, C., Smolyar, I, and Locarini, R., 2019, World Ocean Atlas 2018, Volume 1: Temperature, 52 p.

Lofverstrom, M., Thompson, D. M., Otto-Bliesner, B. L., and Brady, E. C., 2022, The importance of Canadian Arctic archipelago gateways for glacial expansion in Scandinavia: Nature Geoscience, v. 15, p. 482–488. DOI: 10.1038/s41561-022-00956-9.

Lohmann, G. P., 1995, A model for variation in the chemistry of planktonic foraminifera due to secondary calcification and selective dissolution: Paleoceanography, v. 10, p. 445–457. DOI: 10.1029/95PA00059.

Malevich, S. B., Vetter, L., and Tierney, J. E., 2019, Global core top calibration of 18 o in planktic foraminifera to sea surface temperature: Paleoceanography and Paleoclimatology, v. 34, p. 1292–1315. DOI: 10.1029/2019PA003576.

McKay, N. P., Kaufman, D. S., Routson, C. C., Erb, M. P., and Zander, P. D., 2018, The onset and rate of Holocene neoglacial cooling in the Arctic: Geophysical Research Letters, v. 45, p. 12,487–12,496. DOI: 10.1029/2018GL079773.

Natland, M. L., 1938, New species of Foraminifera from off the West Coast of North America and from the Later Tertiary of the Los Angeles Basin: Bulletin of the Scripps Institute of Oceanography, v. 4, p. 137–164.

Nørgaard-Pedersen, N., Spielhagen, R. F., Erlenkeuser, H., Grootes, P. M., Heinemeier, J., and Knies, J., 2003, Arctic Ocean during the last glacial maximum: Atlantic and polar domains of surface water mass distribution and ice cover: Paleoceanography, v. 18. DOI: 10.1029/2002pa000781.

Nürnberg, D., Bijma, J., and Hemleben, C., 1996, Assessing the reliability of magnesium in foraminiferal calcite as a proxy for water mass temperatures: Geochimica et Cosmochimica Acta, v. 60, p. 803–814. DOI: 10.1016/0016-7037(95)00446-7.

Ovechkina, M. N., Bylinskaya, M. E., and Uken, R., 2010, Planktic foraminiferal assemblage in surface sediments from the Thukela Shelf, South Africa: African Invertebrates, v. 51, p. 231–254. DOI: 10.5733/afin.051.0202.

Pados, T., and Spielhagen, R. F., 2014, Species distribution and depth habitat of recent planktic foraminifera in Fram Strait, Arctic Ocean: Polar Research, v. 33. DOI: 10.3402/polar.v33.22483.

Parker, F. L., 1962, Planktonic foraminiferal species in Pacific sediments: Micropaleontology, v. 8, p. 219–254.

The participants of ARK-VIII/3, 1992, ARCTIC '91: The expedition ARK-VIII/3 of RV Polarstern in 1991, Fütterer, D. K. (ed.), Alfred-Wegener-Institut für Polarund Meeresforschung, 268 p., ISSN: 0176-5027.

Pnyushkov, A.V., and I.V. Polyakov, 2022, Nansen and Amundsen Basins Observational System (NABOS): Contributing to understanding changes in the Arctic: Oceanography, v. 35(3–4), p. 90–93. DOI: 10.5670/oceanog.2022.104.

Polyak, L., Bischof, J., Ortiz, J. D., Darby, D. A., Channell, J. E., Xuan, C., Kaufman, D. S., Lovlie, R., Schneider, D. A., Eberl, D. D., Adler, R. E., and Council, E. A., 2009, Late Quaternary stratigraphy and sedimentation patterns in the western Arctic Ocean: Global and Planetary Change, v. 68, p. 5–17. DOI: 10.1016/j.gloplacha.2009.03.014.

Poore, R. Z., Ostermann, D. R., and McGeehin, J., 1999, Stable isotope data and AMS 14C dates from Arctic Ocean Section 1994 surface sediment transect and box core samples from the Mendeleyev Ridge area: Open-file Report, United States Geological Survey, 17 p,. DOI: 10.3133/ofr9948.

Proshutinsky, A., Krishfield, R., Toole, J. M., Timmermans, M.-L., Williams, W., Zimmermann, S., Yamamoto-Kawai, M., Armitage, T. W. K., Dukhovsky, D., Golubeva, E., Manucharyan, G. E., Platov, G., Watanabe, E., Kikuchi, T., Nishino, S., Itoh, M., Kang, S.-H., Cho, K.-H., and Zhao, J., 2019, December, Analysis of the Beaufort Gyre freshwater content in 2003-2018: Journal of Geophysical Research: Oceans, v. 124, p. 9658–9689. DOI: 10.1029/2019JC015281.

Rabe, B., and Wisotzki, A., 2010, Physical oceanography during Polarstern cruise ARK-XXIII/3 (AMEX I): Alfred Wegener Institute, Helmholtz Centre for Polar and Marine Research, Bremerhaven, PANGAEA. DOI: 10.1594/PANGAEA.733425.

Rantanen, M., Karpechko, A.Y., Lipponen, A., Nordling, K., Hyvärinen, O., Ruosteenoja, K., Vihma, T., and Laaksonen, A., 2022, Arctic has warmed nearly four times faster than the globe since 1979: Communications Earth and Environment, v. 3, p. 168. DOI: 10.1038/s43247-022-00498-3.

Rayner, N. A., Parker, D. E., Horton, E. B., Folland, C. K., Alexander, L. V., Rowell, D. P., Kent, E. C., and Kaplan, A., 2003, Global analyses of sea surface temperature, sea ice, and night marine air temperature since the late nineteenth century: Journal of Geophysical Research, v. 108, p. 4407. DOI: 10.1029/2002JD002670.

Risebrobakken, B., and Berben, S. M. P., 2018, Early Holocene establishment of the Barents Sea Arctic Front: Frontiers in Earth Science, v. 6. DOI: 10.3389/feart.2018.00166.

Romanova, A., Anin, V., Pletnev, S., and Tarasova, T., 2017, Carbonate dissolution and ultrastructural breakdown in planktonic foraminifera in the sea of Okhotsk.

Ruddiman, W. F., 1969, Recent planktonic foraminifera: Dominance and diversity in North Atlantic surface sediments: Science, v. 164, p. 1164–1167. DOI: 10.1126/science.164.3884.116.

Schaefer, J. M., Finkel, R. C., Balco, G., Alley, R. B., Caffee, M. W., Briner, J. P., Young, N. E., Gow, A. J., and Schwartz, R., 2016, Greenland was nearly ice-free for extended periods during the Pleistocene: Nature, v. 540, p. 252–255. DOI: 10.1038/nature20146.

Schiebel, R., and Hemleben, C., 2005, Modern planktic foraminifera: Paläontologische Zeitschrift, v. 79, p. 135–148. DOI: 10.1007/BF03021758.

Schiebel, R., and Hemleben, C., 2017, Planktic Foraminifers of the Modern Ocean, 2nd ed.: Springer Berlin, Heidelberg, 358 p., ISBN: 978-3-662-57052-4.

Schiebel, R., Spielhagen, R. F., Garnier, J., Hagemann, J., Howa, H., Jentzen, A., Martínez-Garcia, A., Meilland, J., Michel, E., Repschläger, J., Salter, I., Yamasaki, M., and Haug, G., 2017, Modern planktic foraminifers in the high-latitude ocean: Marine Micropaleontology, v. 136, p. 1–13. DOI: 10.1016/j.marmicro.2017.08.004.

Schrag, D. P., 1999, April, Rapid analysis of high-precision Sr/Ca ratios in corals and other marine carbonates: Paleoceanography, v. 14, p. 97–102. DOI: 10.1029/1998PA900025.

Semiletov, I., 2005, The East Siberian Sea as a transition zone between Pacific-derived waters and Arctic shelf waters: Geophysics Research Letters, v. 32. DOI: 10.1029/2005GL022490.

Simstich, J., Sarnthein, M., and Erlenkeuser, H., 2003, Paired $\delta^{18}O$ signals of *Neogloboquadrina pachyderma* and *Turborotalita quinqueloba* show thermal stratification structure in Nordic Seas: Marine Micropaleontology, v. 48, p. 107–125. DOI: 10.1016/S0377-8398(02)00165-2.

Soltwedel, T., Hasemann, C., Vedenin, A., Bergmann, M., Taylor, J., and Krauß, F., 2019, Bioturbation rates in the deep Fram Strait: Results from in situ experiments at the Arctic LTER observatory HAUSGARTEN: Journal of Experimental Marine Biology and Ecology, v. 511, p. 1–9. DOI: 10.1016/j.jembe.2018.11.001.

Spielhagen, R. F., and Erlenkeuser, H., 1994, Stable oxygen and carbon isotopes in planktic foraminifers from Arctic Ocean surface sediments: Reflection of the low salinity surface water layer: Marine Geology, v. 119, p. 227–250. DOI: 10.1016/0025-3227(94)90183-x.

Stuiver, M., and Reimer, P. J., 1993, Extended ^{14}C database and revised Calib radiocarbon calibration program: Radiocarbon, v. 35, p. 215–230. DOI: 10.1017/S0033822200013904.

SWERUS scientific party, 2016, Cruise report swerus-c3 leg 2: Stockholms Universitet, Stockholm, 190 p., ISBN: 978-91-87355-21-9.

Swift, J., 2006, Physical oceanography at CTD station AOS94/20-1: Scripps Institution of Oceanography, UC San Diego, PANGAEA. DOI: 10.1594/PANGAEA.476041.

Tell, F., Jonkers, L., Meilland, J., and Kucera, M., 2022, Upper-ocean flux of biogenic calcite produced by the Arctic planktonic foraminifera *Neogloboquadrina pachyderma*: Biogeosciences, v. 19, p. 4903–4927. DOI: 10.5194/bg-19-4903-2022.

Thirumalai, K., Quinn, T. M., and Marino, G., 2016, Constraining past seawater $\delta^{18}O$ and temperature records developed from foraminiferal geochemistry: Paleoceanography, v. 31, p. 1409–1422. DOI: 10.1002/2016PA002970.

Thunell, R. C., 1976, Sep, Optimum indices of calcium carbonate dissolution, in deep-sea sediments: Geology, v. 4, p. 525–528. DOI: 10.1130/0091-7613(1976)4<525:OIOCCD>2.0.CO;2.

Tierney, J. E., Malevich, S. B., Gray, W., Vetter, L., and Thirumalai, K., 2019, Bayesian calibration of the mg/ca paleothermometer in planktic foraminifera: Paleoceanography and Paleoclimatology, v. 34, p. 2005–2030. DOI: 10.1029/2019PA003744.

Tierney, J., Pausata, F. & deMenocal, P., 2015, Deglacial Indian monsoon failure and North Atlantic stadials linked by Indian Ocean surface cooling: Nature Geoscience, v. 9, p. 46–50. DOI: 10.1038/ngeo2603.

Timmermans, M.-L., and Marshall, J., 2020, Understanding Arctic Ocean circulation: A review of ocean dynamics in a changing climate: Journal of Geophysical Research: Oceans, v. 125. DOI: 10.1029/2018JC014378.

Vihma, T., 2014, Effects of Arctic sea ice decline on weather and climate: A review: Surveys in Geophysics, v. 35, p. 1175–1214. DOI: 10.1007/s10712-014-9284-0.

Volkmann, R., 2000, Planktic foraminifers in the outer Laptev Sea and the Fram Strait–modern distribution and ecology: Journal of Foraminiferal Research, v. 30, p. 157–176. DOI: 10.2113/0300157.

Volkmann, R., and Mensch, M., 2001, Stable isotope composition ($\delta^{18}O$, $\delta^{13}C$) of living planktic foraminifers in the outer Laptev Sea and the Fram Strait: Marine Micropaleontology, v. 26, p. 163–188. DOI: 10.1016/S0377-8398(01)00018-4.

Vázquez Riveiros, N., Govin, A., Waelbroeck, C., Mackensen, A., Michel, E., Moreira, S., Bouinot, T., Caillon, N., Orgun, A., and Brandon, M, 2016, Mg/Ca thermometry in planktic foraminifera: Improving paleotemperature estimations for *G. bulloides* and *N. pachyderma* left: Geochemistry, Geophysics, Geosystems, v. 17, p. 1249–1264. DOI: 10.1002/2015GC006.

Wang, X., Zhao, J., Lobanov, V. B., Kaplunenko, D., Rudykh, Y. N., He, Y., and Chen, X., 2021, Distribution and transport of water masses in the East Siberian Sea and their impacts on the Arctic halocline: Journal of Geophysical Research: Oceans, v. 126. DOI: 10.1029/2020jc016523.

Werner, K., Spielhagen, R. F., Bauch, D., Hass, H. C., and Kandiano, E., 2013, Atlantic water advection versus sea-ice advances in the eastern Fram Strait during the last 9 ka: Multiproxy evidence for a two-phase Holocene: Paleoceanography, v. 28, p. 283–295. DOI: 10.1002/palo.20028.

Xiao, W., Wang, R., Polyak, L., Astakhov, A., and Cheng, X., 2014, Stable oxygen and carbon isotopes in planktonic foraminifera *Neogloboquadrina pachyderma* in the Arctic Ocean: An overview of published and new surface-sediment data: Marine Geology, v. 352, p. 397–408. DOI: 10.1016/j.margeo.2014.03.024.

Zahn, R., Markussen, B., and Thiede, J., 1985, Stable isotope data and depositional environments in the late Quaternary Arctic Ocean: Nature, v. 314, p. 433–435. DOI: 10.1038/314433a0.

Zehnich, M., Spielhagen, R. F., Bauch, H. A., Forwick, M., Hass, H. C., Palme, T., Stein, R., and Syring, N., 2020, Environmental variability off NE Greenland (western Fram Strait) during the past 10,600 years: The Holocene, v. 30, p. 1752–1766. DOI: 10.1177/0959683620950393.

Zweng, M., Reagan, J. R., Seidov, D., Boyer, T., Locarnini, M., Garcia, H., Mishonov, A. V., Paver, C., and Smolyar, I., 2019, World Ocean Atlas 2018, Volume 2: Salinity: A. Mishonov (ed.), NOAA Atlas NESDIS 82, Silver Spring, MD, 50 p.

Received 7 December 2022
Accepted 23 June 2023

APPENDIX CAPTIONS

Table A1. The number of samples relevant to this study per run are reported in conjunction with the number of standards used to calibrate the run and the average stable isotopic ratios of the standards for the run.

Figure A1. An illustration of the primary bathymetric features mentioned in this study relative to core sites. Pink circles represent this study, orange triangles represent previous studies.

Figure A2. a) Average annual sea surface temperature. b) Average annual sea surface salinity. c) Forward-modeled average annual $\delta^{18}O_{calcite}$ at 0 m.

Figure A3. a) Average annual temperature at 100 m. b) Average annual salinity at 100 m. c) Forward-modeled average annual $\delta^{18}O_{calcite}$ at 100 m.

Figure A4. Top: a) Average annual temperature at 150 m. b) Average annual salinity at 150 m. Bottom: a) Average annual temperature at 200 m. b) Average annual salinity at 200 m.

Figure A5. SEM images of *Nps-2* at each core site. Benthic-planktic ratios and relative grades described in *Materials and Methods* shown for corresponding images. Sites are arranged by proximity to the Bering Strait.

Figure A6. Output from BayFox. Reconstructed temperature for all sites.

Figure A7. Differences between forward-modeled $\delta^{18}O$ and observed $\delta^{18}O$ from N. pachyderma during a) DJF, b) MAM, c) JJA, and d) SON. Points closer to the bold dashed line at zero indicate more similarity between modeled and measured values.

Figure A8. Seawater temperature (pink circles, top plot, left axis) at each core site (arranged in proximity to the Bering Strait) reconstructed from *Nps-2* Mg/Ca data (Eqn. 3). Dashed lines (right axis) show WOA temperature data at 0–200 m for a) DJF, b) MAM, c) JJA, and d) SON. Salinity (blue circles, bottom plot, left axis) calculated using reconstructed temperature (Eqn. 3) and *Nps-2* $\delta^{18}O$ (Eqn. 2) for a) DJF, b) MAM, c) JJA, and d) SON. Dashed lines (right axis) represent WOA salinity data. Depths are labeled accordingly.

Figure A9. All backscattered electron images show the umbilical view of unencrusted foraminiferal outliers. Images 1a, 5a, 7a, 12a, and 16a show high magnification views of test ultrastructure. Images 1-3 are from site PS2185. Images 4-15 and 17-19 are from site PS2170. Image 16 is from site SWE22.

Figure A10. Examples of *N. incompta* morphological variability from sites PS2170 and PS2185. All images utilize back scattered electron methodology.

Figure A11. Examples of kummerforms of *N. pachyderma* with secondary individuals attached to the penultimate chamber. All images utilize back scattered electron methodology.

Cushman Foundation for Foraminiferal Research
Est. 1950